Crustal structure beneath the Strait of Juan de Fuca and southern Vancouver Island from seismic and gravity analyses

D. Graindorge,[1] G. Spence,[2] P. Charvis,[1] J. Y. Collot,[1] R. Hyndman,[3] and A. M. Tréhu[4]

[1] Wide-angle and vertical incidence seismic data from Seismic Hazards Investigations in Puget Sound (SHIPS), gravity modeling, and seismicity are used to derive two-dimensional crustal models beneath the Strait of Juan de Fuca. The Eocene volcanic Crescent-Siletz terrane is significantly thicker than previously recognized and extends from near the surface to depths of 22 km or greater. For the northern strait, a weak midcrustal reflector, dipping east from 12- to 22-km depth, is inferred from wide-angle reflections. A stronger deeper reflector, dipping eastward from 23- to 36-km depth, is associated with the top of "reflector band E," a zone of high reflectivity on coincident Multichannel Seismic (MCS) data, interpreted as a shear zone. A high-velocity zone (7.60 ± 0.2 km s^{-1}) between these reflectors is interpreted as a localized slice of mantle accreted with the overlying Crescent-Siletz terrane. For the southern strait, no deep high-velocity layer is observed and the E-band reflectivity is weaker than to the north. A strong deep reflector, interpreted as the oceanic Moho dips eastward from 35 to 42 km. Seismicity within the subducting slab occurs mainly above the inferred oceanic Moho. Gravity modeling, constrained by the wide-angle seismic models and seismicity, is consistent with the inferred large thickness of Crescent-Siletz and high-density rocks (3030 kg m^{-3}) in the lower crust. *INDEX TERMS:* 1219 Geodesy and Gravity: Local gravity anomalies and crustal structure; 3025 Marine Geology and Geophysics: Marine seismics (0935); 8105 Tectonophysics: Continental margins and sedimentary basins (1212); 9350 Information Related to Geographic Region: North America; 8015 Structural Geology: Local crustal structure; *KEYWORDS:* crustal structure, Juan de Fuca Strait and Vancouver Island, wide-angle seismic, Cascadia subduction zone, Crescent-Siletz terrane, deep crustal reflectivity

1. Introduction

[2] Since 1980, numerous seismic reflection-refraction experiments have been conducted across the margin of Oregon, Washington, and British Columbia to explore the complex velocity and tectonic structure of the Cascadia convergent margin [*Spence et al.*, 1985; *Green et al.*, 1986; *Taber and Lewis*, 1986; *Clowes et al.*, 1987; *Calvert and Clowes*, 1990, 1991; *Hyndman et al.*, 1990; *Tréhu et al.*, 1994; *Calvert*, 1996; *Miller et al.*, 1997; *Flueh et al.*, 1998; *Parsons et al.*, 1998, 1999; *Gerdom et al.*, 2001]. During the Seismic Hazards Investigations in Puget Sound (SHIPS) experiment, conducted in March 1998, onshore-offshore wide-angle data and multichannel reflection data were collected in northwestern Washington State and southwestern British Columbia [*Brocher et al.*, 1999; *Fisher et al.*, 1999]. The objectives were (1) to define the geometry of deep structures that control earthquake occurrence, including the megathrust fault that produces great earthquakes, (2) to provide detailed controls on seismic velocity crustal structure and on crustal faults, and (3) to define sedimentary basins that may affect strong motions during earthquakes.

[3] In this paper we present combined seismic and gravity analyses around the Strait of Juan de Fuca, a 100-km long and 20–25 km wide west-northwest oriented topographic depression, which separates Vancouver Island from the Olympic Peninsula. The analyses are aimed at (1) resolving the velocity structure and thickness of sedimentary basins [*Fisher et al.*, 1999] and the Eocene oceanic Crescent-Siletz terrane, which may be thicker than previously recognized and is thought to be composed of strong crustal blocks of oceanic origin that play an important role in crustal deformation [*Tréhu et al.*, 1994; *Stanley and Villaseñor*, 2000; *Ramachandran*, 2001]; (2) constraining the nature of lower crust high-velocity zones [*Spence et al.*, 1985; *Drew and Clowes*, 1990] and a large reflector band called E that has been interpreted to be a present or former decollement [*Yorath et al.*, 1985; *Calvert*, 1996; *Green et al.*, 1986;

---

[1]UMR Géosciences Azur, Observatoire Océanologique de Villefranche sur Mer, Quai de la Darse, Villefranche sur Mer, France.
[2]School of Earth and Ocean Sciences, University of Victoria, Victoria, British Columbia, Canada.
[3]Pacific Geoscience Center, Geological Survey of Canada, Sidney, British Columbia, Canada.
[4]College of Oceanic and Atmospheric Sciences, Oregon State University, Corvallis, Oregon, USA.

Clowes et al., 1987; *Hyndman*, 1988; *Calvert and Clowes*, 1990; *Hyndman et al.*, 1990]; and (3) determining the geometry of the downgoing oceanic crust and mantle [*Calvert*, 1996] by comparing our results with local microearthquakes. This study using wide-angle data will then test previous interpretations of Crescent-Siletz terrane thickness, of the E reflection and of the geometry of the Moho reflections on the Multichannel Seismic (MCS) data.

[4] This paper complements a regional seismic tomography study [*Ramachandran*, 2001] and MCS data recorded along coincident lines [*Tréhu et al.*, 2002]. Two-dimensional velocity models along the Strait of Juan de Fuca were obtained using simultaneous inversion of travel times from marine air gun shots recorded on land stations. The velocity models are used as constraints to interpret coincident MCS sections, to carry out gravity analyses, and to analyze the relation of the structure to the seismicity distribution in three dimensions.

2. Geological and Tectonic Setting

2.1. Plate Tectonic Setting

[5] The Cascadia continental margin extends from northern California to southern British Columbia (Figure 1). It is associated with the Cascadia magmatic arc onshore and the subducting Juan de Fuca and Gorda plates offshore (Figure 1). Convergence has been the dominant mode of plate interaction along western margin of North America for the past 150 Ma [*Engebretson et al.*, 1992]. Exotic material has been accreted to the margin and then sheared northward during successive episodes of northeast directed oblique convergence and transform motion [e.g., *Riddihough*, 1982]. Two narrow terranes, the Mesozoic mainly sedimentary Pacific Rim and the Eocene volcanic Crescent-Siletz [*Brandon*, 1989], were successively emplaced along the coast at the time of North Pacific plate reorganization at 43 Ma (Figure 2). Currently, the northern Juan de Fuca plate subducts beneath North America at a relative rate of $40-47$ mm a^{-1} directed N56°–68°E [*DeMets et al.*, 1990; *Riddihough and Hyndman*, 1991] (Figure 1).

2.2. Regional Geological and Geophysical Setting

[6] The basic crustal structure in the Vancouver Island region has been investigated in a variety of geological and geophysical studies. Vancouver Island is underlain mainly by rocks of the Wrangellia terrane (part of the Insular superterrane), an accreted package of Devonian through Lower Jurassic igneous sequences, and sedimentary successions [*Wheeler et al.*, 1989; *Journeay and Friedman*, 1993]. On southern Vancouver Island, the Pacific Rim terrane is a metamorphic sediment-rich mélange unit in contact with Wrangellia rocks along the San Juan-Survey fault system (Figure 2).

[7] Crescent formation (also known as Siletz River Volcanics in Oregon and as Metchosin formation on southern Vancouver Island [*Snavely et al.*, 1968; *Massey*, 1986; *Tréhu et al.*, 1994]), which comprises voluminous submarine and subaerial basalts of tholeiitic composition with minor amounts of alkali basalt [*Glassey*, 1974; *Babcock et al.*, 1992], is found at the southern tip of Vancouver Island and the northern Olympic Peninsula (Figure 2). This terrane is thought to have formed as either an accreted oceanic island or a seamount chain [*Duncan*, 1982] or as an accreted oceanic plateau or to have formed in place as the product of a hot spot generated during a continental margin-rifting event [*Babcock et al.*, 1992]. The Pacific Rim and Crescent terranes are separated by the Leech River Fault (Figure 2). In central Oregon, Crescent-Siletz volcanics are $25-35$ km thick [*Tréhu et al.*, 1994]. This terrane is thought to thin progressively northward into Washington, where its mapped thickness is more than 16 km [*Babcock et al.*, 1992]. The Crescent-Siletz terrane extends to depths as great as 25 km based on tomographic results [*Symons and Crosson*, 1997; *Van Wagoner et al.*, 2002]. It has previously been interpreted as only 6 km thick offshore Vancouver Island [*Hyndman et al.*, 1990]. Crescent-Siletz terrane provides the backstop to a large accretionary sedimentary prism formed from the sediments scraped off the incoming oceanic plate [*Brandon and Calderwood*, 1990; *Hyndman*, 1995b; *Parsons et al.*, 1999; *Stanley et al.*, 1999] (Figure 2).

[8] An important feature of the lower crust beneath Vancouver Island, first detected on Lithoprobe Vibroseis seismic reflection lines across Vancouver Island, is a $5-8$ km thick band of high reflectivity which dips eastward from around 20 to 33 km depth [*Yorath et al.*, 1985] (Figure 2). There have been a variety of subduction-related interpretations for the origin of this reflective layer, generally referred to as the "E" reflectivity band. *Calvert and Clowes* [1990] and *Calvert* [1996] argue that it is a structural feature associated with a lower crustal shear zone, while *Hyndman* [1988] and *Kurtz et al.* [1990] suggest that the reflectivity is produced by fluid-filled porosity within sediment or mafic materials that have been deeply subducted.

[9] Velocities >7.0 km s^{-1} have been interpreted by *Spence et al.* [1985] to overlie the lower crustal reflective band. Beneath Vancouver Island several interpretations for the high-velocity zone have been proposed, including (1) a detached piece of oceanic lithosphere accreted during an episodic event [*Green et al.*, 1986] and (2) imbricated mafic rocks derived from the top of the subducting oceanic crust by continuous accretion [*Clowes et al.*, 1987; *Fuis*, 1998].

2.3. Seismicity

[10] In the past century, few subduction zones have exhibited such low recurrence rates for large earthquakes as Cascadia. Prior to the M_w 6.8 Nisqually event in 2001 [*Malone et al.*, 2001], no subduction earthquake of moment magnitude (M_w) larger than 6 has occurred there for the past 70 years [*Kanamori and Heaton*, 1996], and no great interplate event has occurred within recorded history [*Rogers*, 1988; *Dewey et al.*, 1989]. However, the Cascadia subduction zone has many characteristics in common with those along which large interplate earthquakes occur [*Heaton and Hartzell*, 1987; *Rogers*, 1988]. Furthermore, many lines of evidence provide strong support for the occurrence of great thrust events at an average interval of 600 years, with the last event occurring in 1700 [*Atwater*, 1987, 1992; *Hyndman*, 1995a; *Satake et al.*, 1996; *Goldfinger et al.*, 1999] (Figure 1). Most current seismicity in the Cascadia forearc of southern British Columbia and Washington is concentrated around Puget Sound and the eastern Strait of Juan de Fuca [*Ludwin et al.*, 1991]. The margin seismicity includes (1) events within the continental crust occurring in the Puget Sound-Georgia
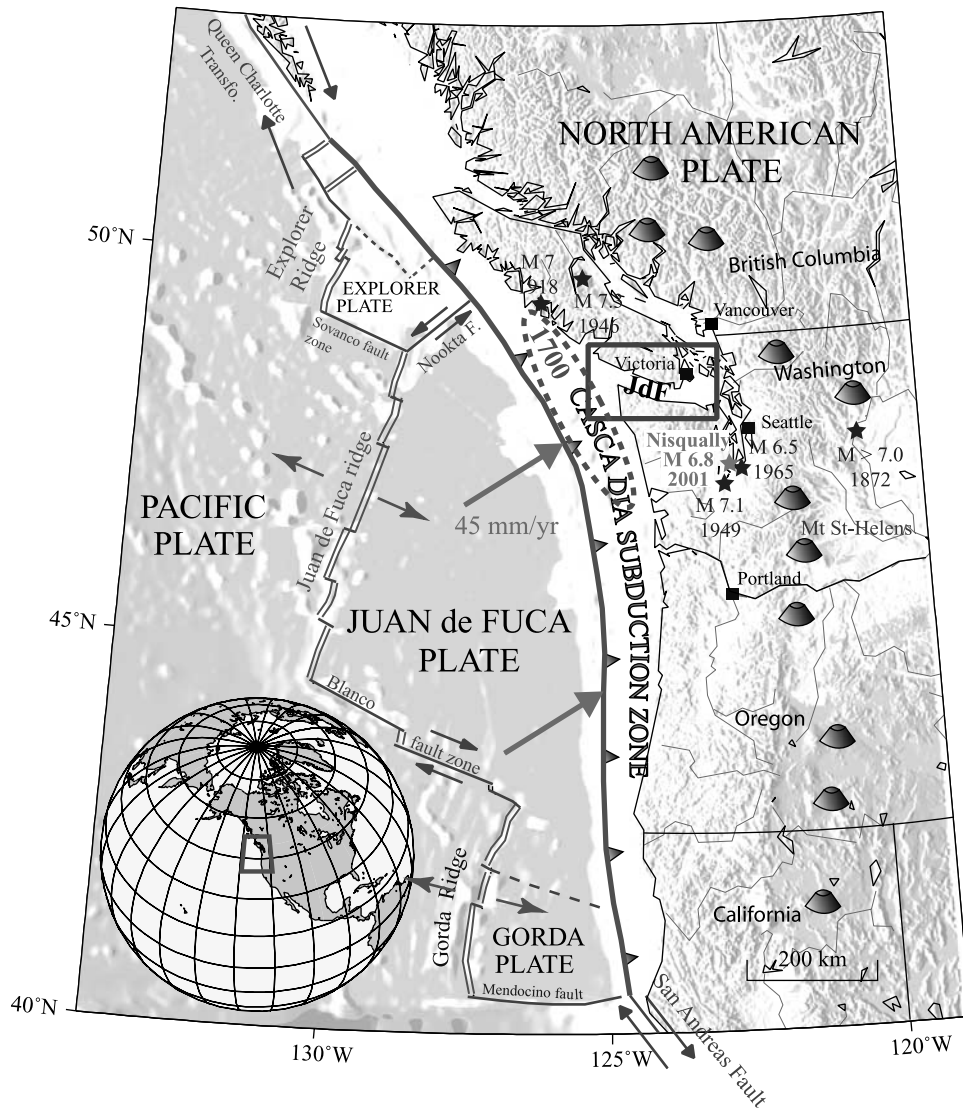
Figure 1. Map of the Cascadia Subduction Zone showing the Juan de Fuca plate offshore and the volcanic arc on the North American plate. Stars indicate the largest earthquakes recorded. The ellipse indicates the rupture zone of the inferred 1700 large earthquake. The rectangle delimits the study area around the Strait of Juan de Fuca.

Strait area, associated with north-south shortening that accommodates arc-parallel migration of an Oregon forearc block in response to oblique subduction [*Wang*, 1996; *Wells et al.*, 1998; *Khazaradze et al.*, 1999; *Mazzotti et al.*, 2002] and (2) Benioff zone earthquakes.

3. Data

3.1. Seismic Data

3.1.1. Wide-Angle Data

[11] The wide-angle data presented here were recorded during the 1998 SHIPS experiment. SHIPS was conducted within and near Puget Sound, the Strait of Juan de Fuca, Hood Canal, and Georgia Strait (Figure 1). The R/V *Thomas G. Thompson* towed the air gun sources and recorded MCS data [*Brocher et al.*, 1999; *Fisher et al.*, 1999]. In this study, we interpret data mainly from three shot profiles (lines 4, 7, and 8) fired along the Strait of Juan de Fuca (Figure 2). During wide-angle surveying, a 110 L array was fired approximately every 40 s (line 4), while during the MCS survey, an 85 L array was fired every 20 s (lines 7 and 8). DFS-V field recording instruments were used to collect 24-fold, 16 s data from the 96-channel, 2500-m streamer [*Fisher et al.*, 1999]. The large air gun arrays were recorded by more than 250 onland seismographs. Stations were REFTEK recorders containing either an oriented three components or a single vertical seismometer [*Brocher et al.*, 1999]. Reftek station locations and elevations are given by *Brocher et al.* [1999]. Table 1 provides a list of station names used in this study versus their names in the work by *Brocher et al.* [1999].

[12] We selected recorders located near the ship's tracks to provide quasi two-dimensional lines, although the curvature of the waterways precluded purely linear profiles [*Brocher et al.*, 1999]. For this study, we used five stations
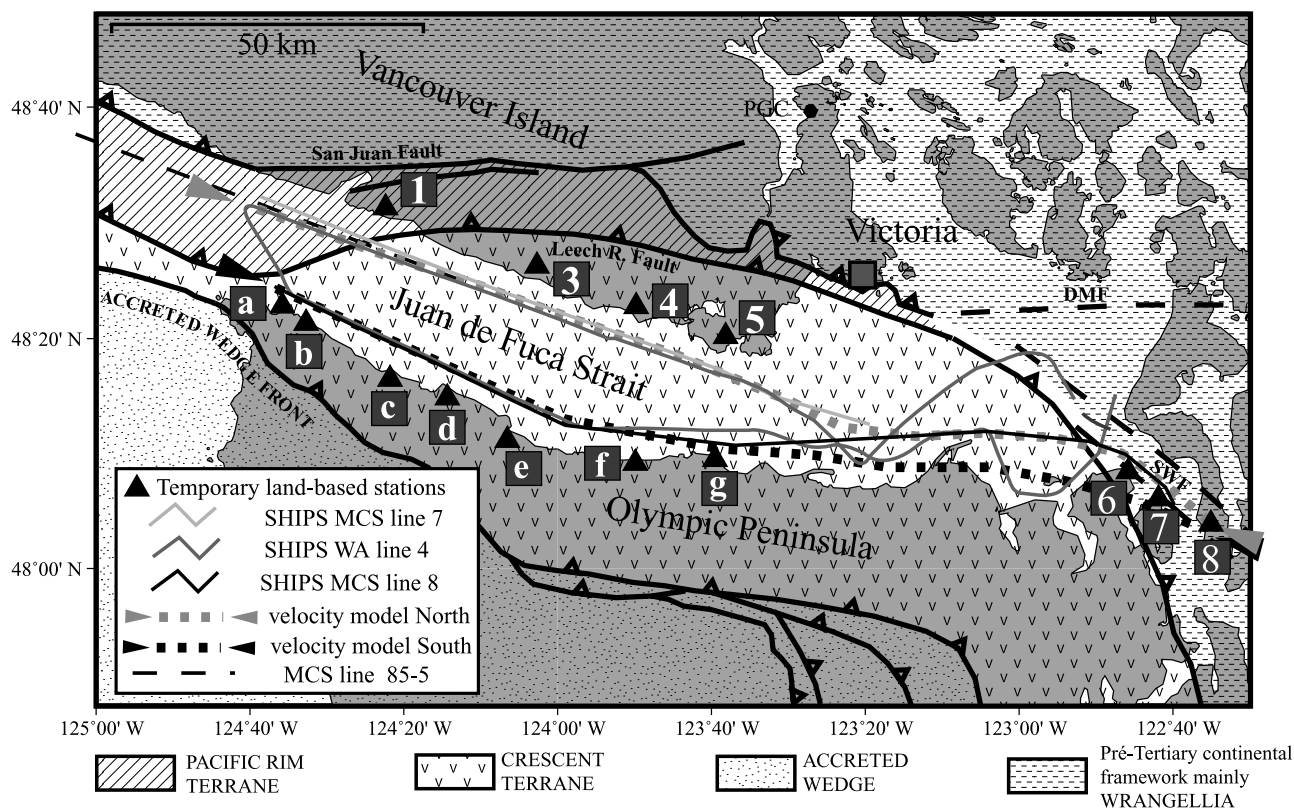
Figure 2. Principal geological units in study: accreted wedge, Crescent terrane, Pacific Rim terrane, and pre-Tertiary continental framework. The triangles are locations of land-based stations used in the travel time modeling of wide-angle arrivals. Shaded lines indicate MCS profiles, and ship track lines of the SHIPS indicate seismic reflection survey. DMF, Devils Mountain Fault; SWF, Southern Whidbey Island Fault.

from southern Vancouver Island, seven stations from northern and northeastern Olympic Peninsula, and three stations from northern Puget Sound. To reduce three-dimensional effects, we ignored all arrivals with an offset less than 7 km. We kept 20 s of the signal of the vertical component of data with the time of the first sample controlled by offset and a reducing velocity of 8 km s^{-1}. A Butterworth band-pass filter with limits of 5 and 15 Hz was applied. The amplitude of each trace was normalized by the square root of offset.

[13] We applied a small single static shift to each profile to correct for the differing elevations of each receiver station. A limitation of the two-dimensional modeling approach for this type of onshore-offshore data set is that the receiver and the nearest shots are at the same position in the model, but the receiver is on land and the shots are in water. Thus we applied a correction that substituted a water layer (velocity 1.5 km s^{-1}) for the equivalent layer of solid rock that lay beneath the receiver. All stations were on or near bedrock, so we assumed a near-surface rock velocity of 6 km s^{-1}, based on the near-offset apparent velocities on the recorded profiles. For the correction, we assumed a phase velocity of 6.5 km s^{-1}, approximately the mean of the observed phase velocities that ranged from 6.0 to 7.2 km s^{-1}. For each station, the static correction simulates a model in which the receiver is located in water at sea level, with water depth given by the depth at the closest shot. A typical

correction was 120 ms, and so errors in the assumptions will result in uncertainties that are much less than the smallest picking error of 50 ms.

3.1.2. Wide-Angle Modeling Procedure

[14] The velocity models were developed through a combination of travel time inversion and amplitude modeling of both wide-angle reflections and refractions. Empirical raytrace forward modeling was first applied to get an

Table 1. List of Station Names Used in This Study Versus Their Names as Given by *Brocher et al.* [1999]

Stations Names Used in This Study	Station Names Given by *Brocher et al.* [1999]
1	CA01
2	CA02
3	CA03
4	CA04
5	CA05
6	OR03
7	OR01
8	1016
A	OR25
B	OR24
C	OR22
D	OR21
E	OR19
F	OR17
G	OR14

Table 2. Observed Phases and Travel Time Fits for Deep-Crustal Northern Model

Layer	Phases	Instruments	Pick Uncertainty, s	Travel Time Fits		
				Number of Travel Times	RMS Misfit, s	Normalized χ^2
3	$P1$	7, 8	0.050	261	0.084	1.951
4	Pg	1, 3, 4, 5, 6, 7, 8	0.070	4698	0.128	3.35
4	$Pr1$	1, 3, 4, 5, 6, 7, 8	0.200	802	0.201	1.012
5	$Pr2$	1, 3, 4, 5, 6, 7, 8	0.150	1591	0.202	1.822

acceptable starting model that roughly matches the observed and calculated travel times. The travel times were then inverted using the raytrace-based inversion scheme of *Zelt and Smith* [1992]. This inversion is performed in a layer-stripping fashion, where the parameters of successively deeper layers are determined while the parameters defining the shallower layers remain fixed. First, arrival and reflection travel times recorded on the land stations were digitized, and uncertainties which depend on signal-to-noise ratios were estimated (Tables 2 and 3).

[15] The hybrid procedure used to derive models consisted of (1) determination of the water depth and sediment layer thicknesses from coincident MCS data (we used a mean velocity of 2.2 km s^{-1} since the average sediment velocities determined from travel times of the near-offset arrivals ranged from 2.0 to 3.5 km s^{-1}); (2) travel time inversion of upper middle crustal turning waves (phase Pg); (3) travel time inversion of deeper reflected arrivals; and (4) adjustment of the velocity contrasts across the midcrust to lower crust reflectors via amplitude modeling and subsequent iteration through the travel time inversion of steps 2–3.

[16] We assessed the quality of the velocity model using four measures: the uncertainty of the travel time picks, the goodness of fit between predicted and observed travel times, the resolution of velocity and interface nodes related to the ray coverage (Figures 5 and 10 and Tables 2 and 3), and the variability of the model within the model space by comparing Root Mean Squares (RMS) travel time misfits and χ^2 values for a suite of velocity models [*Holbrook et al.*, 1994; *Zelt*, 1999]. The nodes with a resolution value >0.5 are considered to be well resolved [*Zelt and Smith*, 1992]. To evaluate the travel time fits, Trms is the RMS of the misfit between the calculated and observed travel times, and its value should be as close as possible to the uncertainty of the travel time picks. The χ^2 is a dimensionless value representing the RMS of the misfit normalized by the uncertainty of the observed travel times; its value should ideally be close to 1. These statistical measures, presented in Tables 2 and 3, indicate that the formal picking errors may be

unrealistically small and that the parameterization may not be representative of the small-scale variations near the shots and receivers. For amplitude modeling, synthetic seismograms were calculated using zero-order asymptotic ray theory [*Cerveny et al.*, 1977]. Modeling of amplitudes aimed to fit the general trends of critical point locations for specific phases, while modeling of relative amplitudes between phases was only qualitative.

3.1.3. MCS Data

[17] SHIPS MCS lines 7 and 8 (Figure 11) are coincident with northern and southern wide-angle models, respectively. Only basic processing including geometrical correction and deconvolution, sorting into common depth point reflection gathers, velocity analysis, Normal Move Out (NMO) correction and stacking, and migration have been applied thus far to these two MCS lines [*Tréhu et al.*, 2002]. Recently, more extensive processing has been carried out, and a portion of the newly processed data is presented by *Nedimovic et al.* [2003]. The westernmost 40 km of SHIPS MCS line 7 is coincident with the eastern portion of interpreted Lithoprobe Vibroseis line 85-05 [*Clowes et al.*, 1987].

3.2. Seismicity Data

[18] Seismicity levels are highest in the eastern Strait of Juan de Fuca and Puget Sound [e.g., *Weaver and Baker*, 1988]. Microearthquakes around the Strait of Juan de Fuca compiled by *Mulder* [1995; also personal communication, 2001] are displayed along three sections perpendicular to the strait (Figures 12 and 13). We used all the events from this catalog with magnitude greater than 1 recorded between the years 1984 and 2000 to have enough events to propose a hypothetical interpretation of the top of the downgoing plate seismicity. Events from 25 km on either side of each section were projected perpendicularly onto the line (Figure 12). Hypocenter locations were determined using a laterally homogeneous model. When earthquakes are relocated in a three-dimensional velocity model derived from SHIPS data, hypocenters change by less than 3 km horizontally and

Table 3. Observed Phases and Travel Time Fits for Deep-Crustal Southern Model

Layer	Phases	Instruments	Pick Uncertainty, s	Travel Time Fits		
				Number of Travel Times	RMS Misfit, s	Normalized χ^2
2	S	d	0.04	20	0.045	1.33
3	$P1$	a, b, c, d, e, f	0.05	149	0.077	2.01
3	$2r$	a, b, c, d	0.250	68	0.252	1.03
4	Pg	a, b, c, d, e, f, g	0.07	852	0.135	3.74
5	$Pr2$	a, b, c, d, e, f, g	0.200	195	0.286	2.06
Moho, 1: 6.4 km s^{-1}	PmP	a, b, c, d, e	0.07	55	0.085	1.51
Moho, 2: 7.1 km s^{-1}	PmP	a, b, c, d, e	0.07	55	0.092	1.77
Moho, 3: 7.6 km s^{-1}	PmP	a, b, c, d, e	0.07	56	0.101	2012

vertically [*Ramachandran*, 2001], and so these values represent reasonable estimates of absolute hypocenter uncertainty for bigger events. However, events with magnitudes ranging from 1.0 to 2.5 are probably fairly poorly located since they are only observed on few stations and uncertainty in depth is more likely greater than 5 km.

3.3. Gravity Data

[19] Gravity data in the Strait of Juan de Fuca region from both the Geological Survey of Canada (GSC) and the U.S. Geological Survey were combined in a consistent manner by C. Lowe (personal communication, 2001). The nominal data spacing is ∼1 km. Offshore free air data are accurate to ±2 mGal, and onshore terrain-corrected Bouguer measurements are accurate to ±1 mGal. We modeled gravity data along the same three profiles (A, B, C) across the Strait of Juan de Fuca used for projection of seismic events (Figure 14). We used the program HYPERMAG, an interactive, 2 and $2^{1/2}$ dimensional forward modeling program from the U.S. Geological Survey [*Saltus and Blakely*, 1993]. The two-dimensional calculations are based on the Talwani algorithm [*Talwani et al.*, 1959]. Gravity curves were determined using a 0.3 by 0.3 min gridding of the gravity data.

4. Northern Model

[20] The northern model is based on a 164-km-long seismic line in the northern and southeastern Strait of Juan de Fuca (Figure 2). To determine our velocity model, we selected stations from southern Vancouver Island and northern Puget Sound: stations 1–8 except 2 which was poor. Three stations (3–5) lie directly on Crescent-Siletz Terrane. The stations were all located near the northern coast of the Strait of Juan de Fuca and were typically less than 5 km from the air gun line. SHIPS lines 4 and 7 were used for the western and the central part of the model and line 8 for the eastern part.

4.1. Wide-Angle Data

[21] In some cases, the data quality provided by the smaller air gun array used for MCS recording was better than that used for the wide-angle recording, probably because the MCS air gun array provided a more impulsive waveform. The noise level on most northern stations was low. Sample records of stations 4 and 5 are shown on Figures 3 and 4.

[22] Three principal phases are observed on the wide-angle data of the northern line: a refraction or turning ray within the upper crust (*Pg*) picked out to offsets of 150 km and reflections from two deep boundaries (*Pr*1 and *Pr*2, Figures 3 and 4a) which can be consistently correlated on all stations. On stations 4 and 5, the *Pg* apparent velocity is 6–6.5 km s^{-1} and the intercept time is 0.2 s, which demonstrates that sediments within the Strait of Juan de Fuca are very thin. The high-amplitude first arrivals, which we can clearly follow to distances of more than 80 km, are the strongest arrivals on the seismic sections. The weak upper reflected wave *Pr*1 is asymptotic to the *Pg* refracted arrival at a distance of more than 80 km on stations 4 and 5. This reflection is interpreted as an arrival from a weak discontinuity at midcrustal depths. In addition, an earlier arrival *P*1

with an apparent velocity of 5 km s^{-1} from near-surface and shallow depth sediments is observed on stations at the eastern end of the line (Figure 4b). The deeper reflection *Pr*2 has a larger amplitude corresponding to a stronger velocity discontinuity at greater depth. We also observe the *S* wave arrival (*Sg*) for the upper crustal layer with an apparent velocity of 3.6 km s^{-1}.

4.2. Velocity Model

[23] Modeling of wide-angle refracted and reflected travel times and amplitudes produced a model of compressional wave (*P*) velocity of the crust below the northern Strait of Juan de Fuca (Figure 5b). Layer 1 represents the seawater. The upper to middle crust (layer 4) consists of a thick, high-velocity layer (6.1–6.3 km s^{-1} at the top of the layer increasing to 7.3–7.5 km s^{-1} at its base at 20–22 km depth with a velocity gradient of ∼0.1–0.15 km s^{-1}). Over the first 90 km of the model, layer 4 is overlain by a thin layer of sediments (layer 2) with velocities of about 2–3 km s^{-1} and with a thickness of a few hundred meters, thickening to the southeast. At the southeast end of the line (model distance 125–160 km), velocities of about 3 km s^{-1} are found at 3-km depth, below which we can identify a third layer (3) with velocities increasing from 4.2–4.6 to 5.5–6.0 km s^{-1} at 6-km depth. Reflector *Pr*1, deepening eastward from 12 to 22 km, represents an interface across which the velocity contrast is very small. Reflector *Pr*2 dips eastward from 23 to 36 km. Inferred layer 5 between *Pr*1 and *Pr*2, 8–12 km in thickness, is characterized by very high velocities ranging from 7.5 to 7.7 km s^{-1}. There are no constraints on velocity structure beneath the deeper reflector (*Pr*2).

4.3. Model Uncertainty

[24] The agreement between observed and predicted travel times is generally satisfactory (Figures 3 and 5). Travel time RMS residuals (misfits) for individual phases (reflected and refracted) range from 0.084 to 0.202 s, comparable to the picking errors that range from 0.050 to 0.200 s (Table 2) (Figure 5a). Amplitudes from synthetic seismograms provide an acceptable fit to the data (Figures 3c and 3d). Relative amplitudes of phases *Pg*, *Pr*1, and *Pr*2 are matched, and location of critical points also fit reasonably well. For the *Pg* phase, synthetic amplitudes at far offsets are too large compared to the observed data, perhaps indicating that the deep velocity gradient is too large; however, a smaller gradient would produce a larger-than-observed *Pr*1 amplitude. Resolution values for velocity and interface nodes were calculated during the inversion of travel times [*Zelt and Smith*, 1992] (Figures 6a and 6b). These values together with the number of ray hits (Figure 5c) provide an estimate of ray coverage within the model and are highly dependent on the model parameterization. Velocities at the top of the basement layer 4 were constrained by both refracted and reflected arrivals and have resolution values >0.75. The weakness of the first reflection *Pr*1 implies a small velocity contrast between crustal layers 4 and 5 (<0.3 km s^{-1}) based on amplitude modeling (Figure 3). Although resolution values are useful indicators, insight into uncertainties in velocity and interface depth is best obtained by comparing RMS travel time misfits and χ^2 values for a suite of velocity models [*Holbrook et al.*, 1994; *Zelt*, 1999]. This analysis is a way to approach model
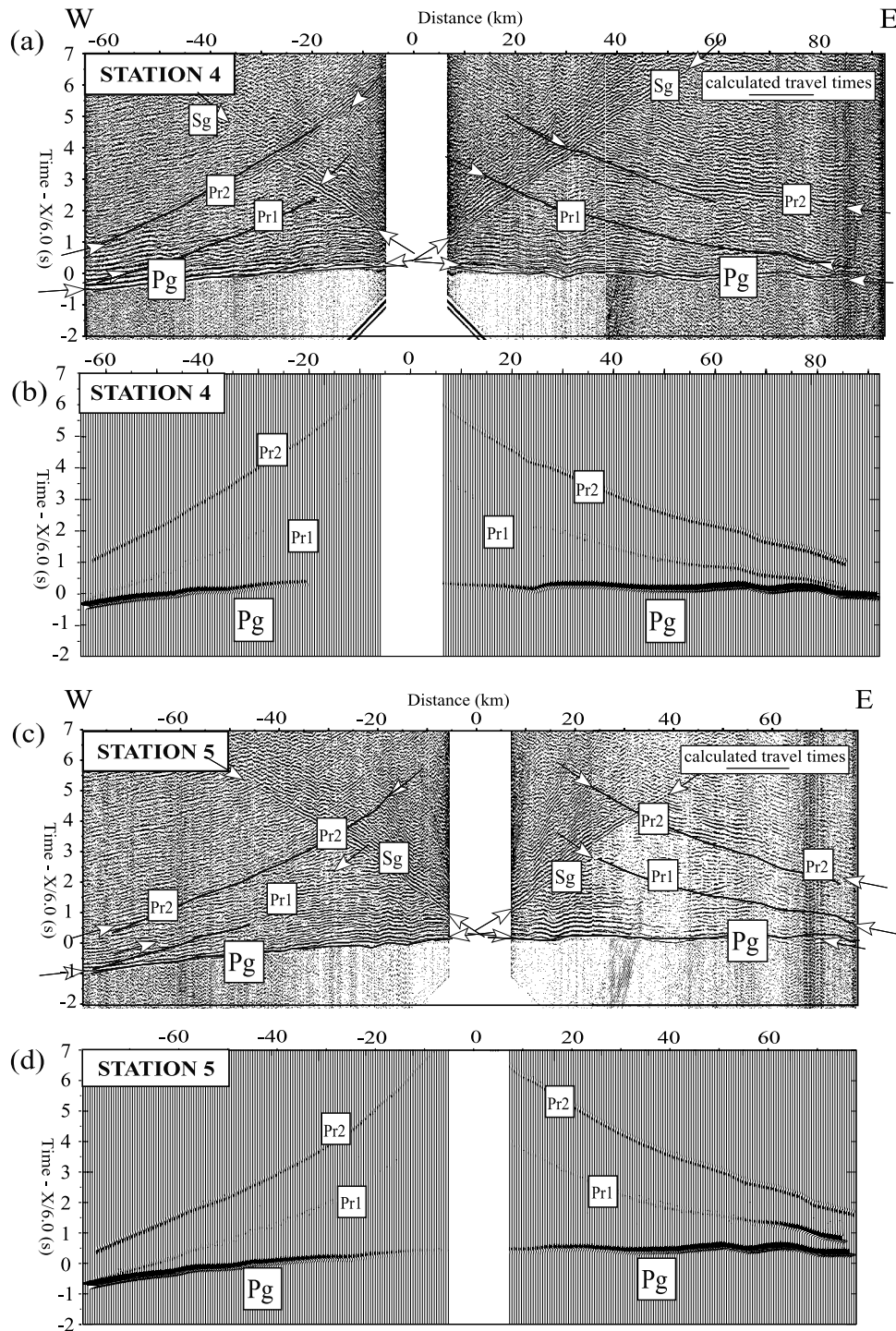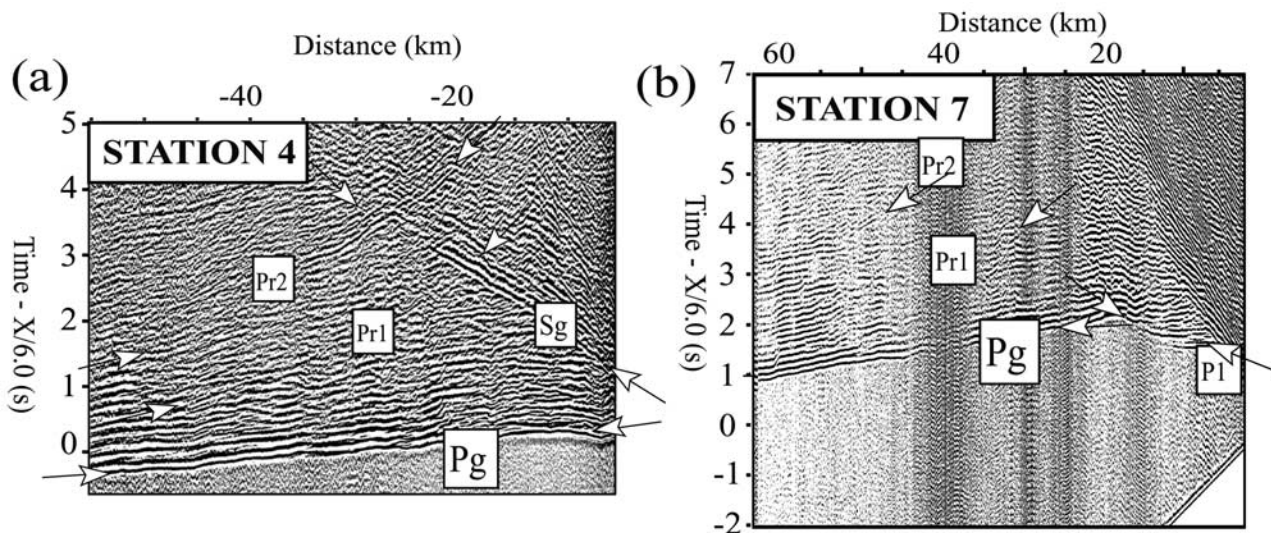
Figure 3. Vertical component wide-angle seismic data for the northern Strait of Juan de Fuca. The refraction profiles are plotted with a reduction velocity of 6 km s^{-1} and a band-pass filter between 5 and 15 Hz, and amplitudes are scaled proportionally to the square root of offset. Labels indicate the different observed phases. Lines represent calculated travel times. For each station, both the observed data and ray theoretical synthetic seismograms, calculated from the final crustal model, are shown: (a) station 4, observed data; (b) station 4, synthetics; (c) station 5, observed data; and (d) station 5, synthetics.

covariance. To explore uncertainty in the velocity at the base of layer 4, we perturbed its value from 7.2 to 7.8 km s^{-1} and then inverted for the best fitting depth of $Pr1$ for each test (Figure 7). For layer 4 arrivals, the RMS misfit and χ^2 are clearly minimized at a value of 7.5 ± 0.1 km s^{-1}. This limited approach, however, provides only a set of perturbations of the final model, not an analysis of all possible models.

Figure 4. Vertical component wide-angle seismic data for the northern Strait of Juan de Fuca. The refraction profiles are plotted with a reduction velocity of 6 km s^{-1} and a band-pass filter between 5 and 15 Hz, and amplitudes are scaled proportionally to the square root of offset. Labels indicate the different observed phases. (a) First 60 km of station 4. (b) First 60 km of station 7 revealing a low-velocity arrival from a basin in the eastern Strait of Juan de Fuca.

[25] For layer 5, between the two deep reflectors $Pr1$ and $Pr2$, the resolution of velocity nodes is poorer, probably because we do not observe arrivals from rays turning within this layer. Nevertheless, through an uncertainty analysis of the layer velocity values, we can demonstrate that the $Pr2$-reflected arrivals provide meaningful velocity constraints. Assuming that the overlying velocity structure is determined, we perturbed the average layer 5 velocities from 6.9 to 8.0 km s^{-1} and observed the corresponding RMS misfits. Velocities less than 6.8 km s^{-1} are not supported since ray paths to many stations could not be found. A velocity of 8.0 km s^{-1} seemed a reasonable upper limit as it represents standard mantle velocity. For a fixed velocity contrast of 0.4 km s^{-1} between the top and bottom of the layer, we inverted for the lower reflector depth that best satisfied the $Pr2$ travel times. The minimum misfit was 0.203 s for an average velocity of 7.6 km s^{-1} (±0.2 km s^{-1}) (Figure 8a). For this average velocity, we tried several values of velocity gradients within the layer (Figure 8b); as expected, there is little constraint on the velocity gradient since no turning rays within the layer were observed.
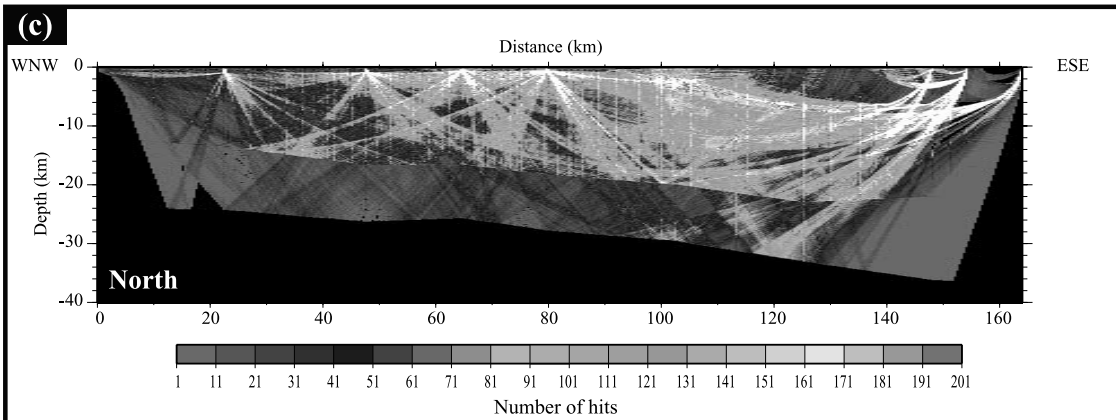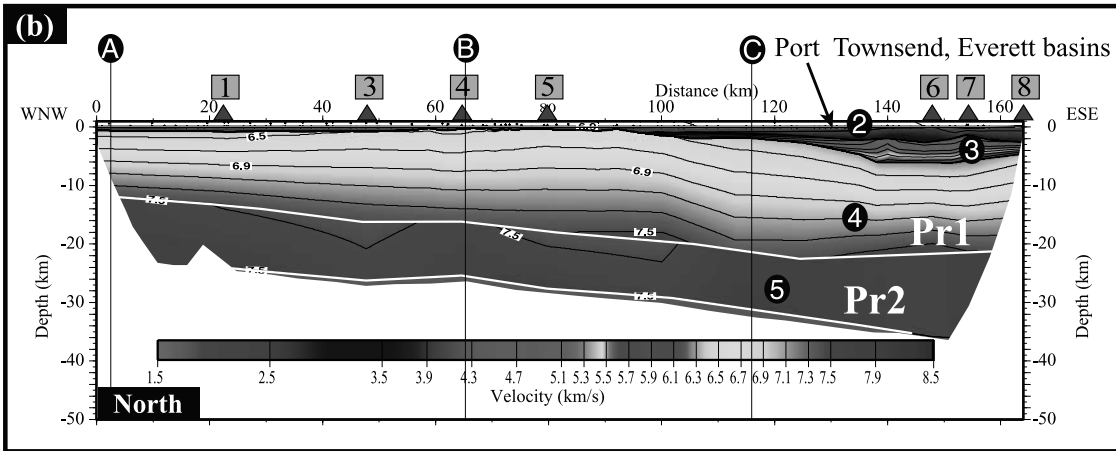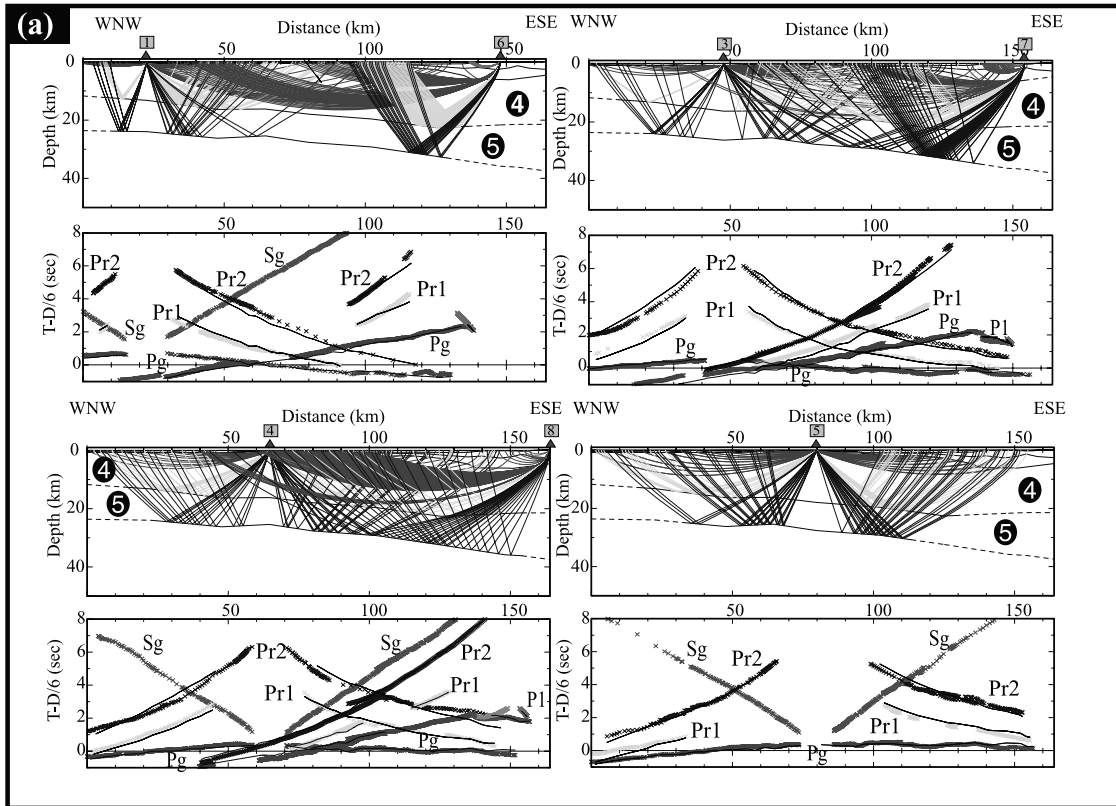
5. Southern Model

[26] The southern line consisted of 157 km of air gun shots (line 8) fired along the southern Strait of Juan de Fuca (Figure 2). We restricted our wide-angle analyses to arrivals at selected Reftek stations a–g deployed on the northern Olympic Peninsula coast. For the first 80 km of the model, the midpoints from shots along line 8 are never offset by more than 2.5 km from the plane of the model. No Olympic Peninsula stations east of station g were used since nearly all arrivals corresponded to out-of-plane ray paths. The southern model was developed using the same procedure as the northern model except that no amplitude modeling and no estimation of uncertainty of deep velocities was carried out because of the complex pattern of deep-reflectivity-inducing uncertainty in the deeper part of the model. The final model was extended eastward to 157 km by combining it with the eastern part of the northern model.

5.1. Wide-Angle Data

[27] On the southern line, arrivals propagated out to offsets of up to 110 km (Figure 9). Five principal phases were observed: a refracted arrival $P1$ from the upper crust with an apparent velocity of 4.0–5.0 km s^{-1}, its associated reflected wave (1r), a refraction or turning wave Pg from the middle crust (Pg) with an apparent velocity of 6.5–7.0 km s^{-1}, and two groups of reflections ($Pr2$ and PmP) from deep boundaries. At station a (Figure 9a), the weak reflected wave 1r appears to be asymptotic with the

Figure 5. (opposite) Northern velocity model. (a) Ray diagrams for the modeled phases and the corresponding observed travel times for stations 1 and 6, 3 and 7, 4 and 8, and 5. The black curves represent calculated travel times. The crosses represent the picked observed arrivals. Different colors correspond to different phases. (b) Velocity model across the northern Strait of Juan de Fuca. Triangles at the top of each velocity model indicate the position of land recording stations. $Pr1$ and $Pr2$ refer to wide-angle deep reflectors. Solid circles with white numbers indicate layer numbers given in text. Solid circles with white letters show the position of seismicity (A, B, C), and gravity sections (A, B) perpendicular to the model and shown in Figures 12–14. (c) Number of ray hits for the northern model, which indicates the ray coverage within the model. White color identifies a number of hits greater than 200. See color version of this figure at back of this issue.
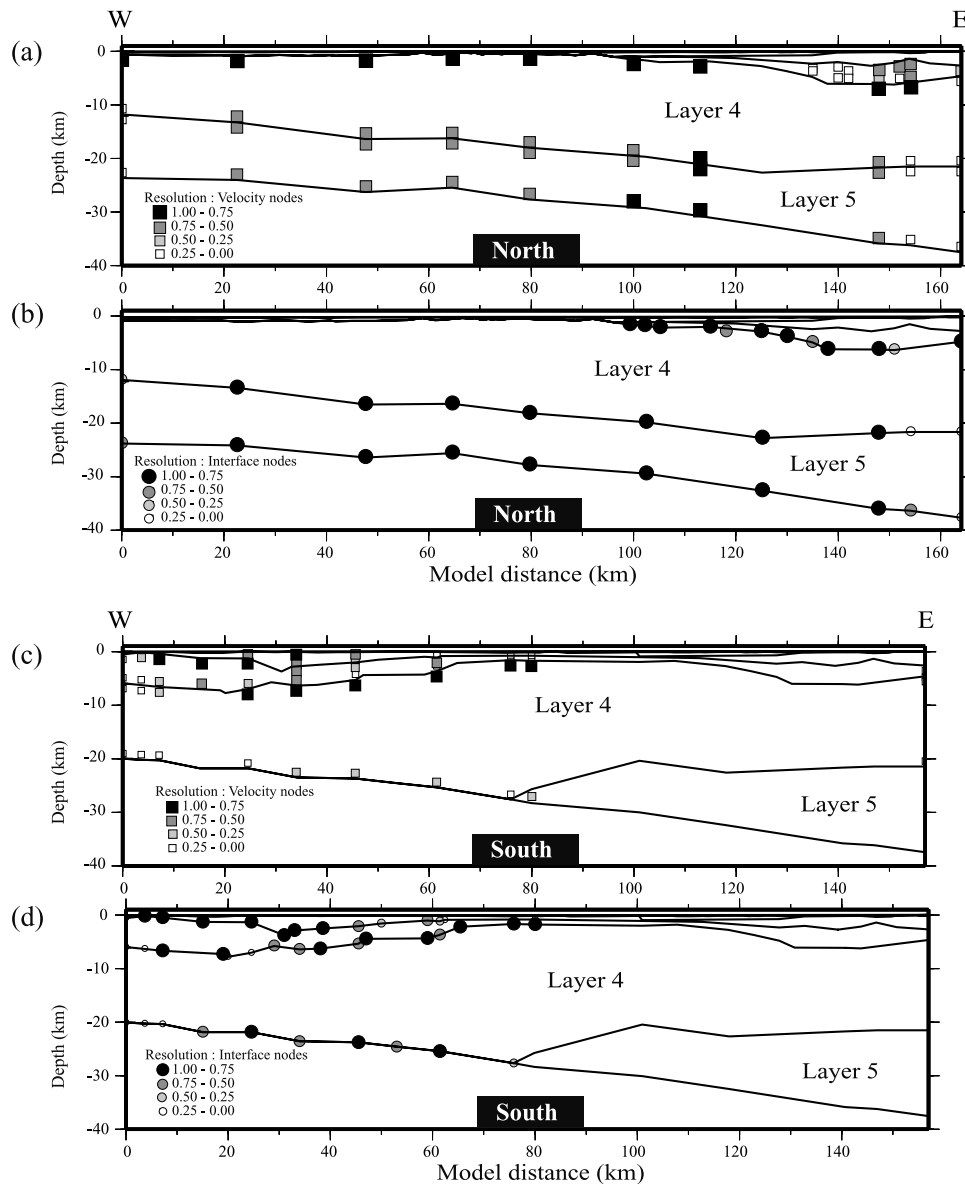
Figure 6. Resolution values calculated from the travel time inversion of the northern velocity model: (a) resolution values of the velocity nodes and (b) resolution values of the interface nodes. Same for the southern model: (c) resolution values of the velocity nodes and (d) resolution values of the interface nodes.

refracted arrival P1 around 25 km. From 25 to 110 km, a strong Pg arrival is observed.

[28] The complex pattern of deep reflectivity, however, did not allow us to consistently correlate arrivals across all stations. There was little evidence of a southern equivalent of Pr1, although there are some scattered low-amplitude reflections. Arrival Pr2 corresponds to a velocity discontinuity from a deep reflector. PmP is a strong reflection which occurs at approximately 3 s and 100 km on station a and at 3.5 s and 100 km on stations e and c (Figure 9b), with an amplitude nearly as large as Pg. This phase PmP clearly arrives after Pr2 at station c (Figure 9c).

5.2. Velocity Model

[29] Wide-angle data modeling produced a compressional P wave velocity model of the crust below the southern Strait

of Juan de Fuca. This model (Figure 10b) consists of an upper layer of seawater (layer 1) underlain by a layer of sedimentary rocks (layer 2) having a maximum thickness of 4 km at around 32-km distance; velocities used for the shallow sedimentary rocks are 2.1 km s^{-1} near the surface, increasing to 3.3 km s^{-1} at the bottom of the layer. Layer 2 is interpreted as a low-velocity sedimentary basin, equivalent to the Clallam basin of *Ramachandran* [2001]. Beneath layer 2, velocities ranging from 3.8 to 5.9 km s^{-1} in layer 3 may correspond to an upper crustal layer composed of older, compacted, or weakly metamorphosed sediments. The thickness of layer 3 reaches 5 km in the west, decreases to less than 1 km between 80 and 110 km, and increases again in the eastern part of the model. In the west, layer 3 of the southern model is equivalent to layer 3 in the northern model.
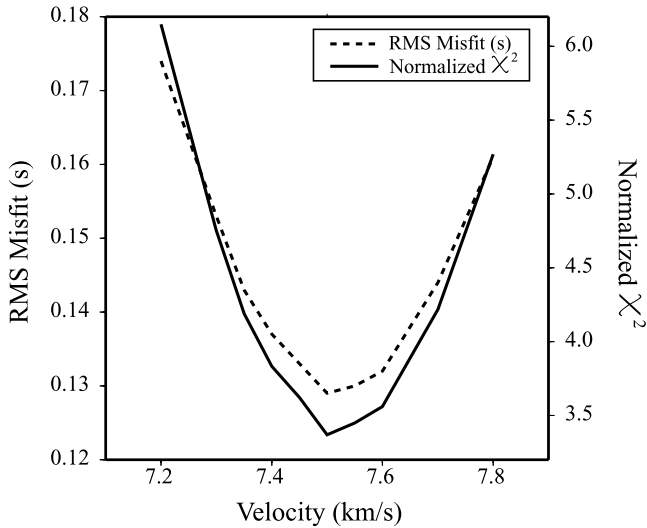
Figure 7. Analysis of uncertainty for the velocity at the base of midcrustal layer 4. The RMS misfit and χ^2 of modeled Pg-refracted arrival travel times is plotted as a function of midcrustal layer 4 velocity. A velocity of $\sim$7.5 km s^{-1} minimizes the RMS misfit while allowing rays to be traced to a large number of observations.

[30]   The upper to middle crust consists of a thick layer (layer 4), with velocities increasing from 6.0–6.2 km s^{-1} at its top to 7.5 km s^{-1} at its base at 20-km depth. A poorly determined wide-angle reflector ($Pr2$) (Table 3 and Figure 10a), deepening from 20-km depth in the northwest to 35 km in the southeast, may represent the base of either layer 4 or 5. Below $Pr2$, the only travel time constraints on velocities can be approached by the observed large amplitude PmP reflections, but there is a large trade-off between Moho depth and the velocity in this unit. We did not explore the full range of model space, but the range was sampled by assigning the region between the $Pr2$ and PmP reflectors three different mean velocities, 6.4, 7.1, and 7.6 km s^{-1}. A velocity of 6.4 km s^{-1} is equivalent to a mean oceanic crust velocity and to the E-layer velocity of 6.4 km s^{-1} derived by *Cassidy* [1995]. A velocity of 7.1 km s^{-1} could represent high-velocity underplated material, such as oceanic rocks [*Fuis*, 1998]. A velocity of 7.6 km s^{-1} was chosen to explore the case of a southern deep continuity of the high velocities, the possible southward extension of the deep high-velocity layer in the northern strait. The PmP reflector ranges in depth from 34 to 39 km in the west and from 41, 43 to 45.5 km in the east (Figure 10b).

5.3. Model Uncertainty

[31]   The generally close agreement between observed and calculated travel times (Figures 9 and 10a) is characterized by the small RMS misfit and χ^2 for each arrival (Table 2). Resolution values of velocity and interface nodes were calculated for the western 80 km of the model (Figures 6c and 6d). Arrivals $P1$ and $1r$ from the deeper portion of layer 3 have small RMS misfits. However, the number of travel times is small, and so the resolution of both velocity and interface nodes

for layer 3 is poor. The number of ray hits (Figure 10c) also indicates that the velocity structure is only adequately constrained down to 15 km. Layer 4, which corresponds to Crescent-Siletz terrane, has the best resolution with a large number of travel times and a RMS misfit of 0.135 s for phase Pg (Table 2). Resolution of the deeper velocity nodes of layer 4 is poorer since offsets are too small to allow deep penetration of turning rays. For arrival $Pr2$, RMS values are relatively large because of the difficulty in picking at all stations (Figure 9). Velocity is only poorly constrained by the PmP travel times, and so the deep structures of the southern model should be viewed with caution. For the three velocities used between the $Pr2$ and PmP reflectors, the PmP arrival has RMS misfits of 0.085, 0.092, and 0.101 s for velocities of 6.4, 7.1, and 7.6 km s^{-1}, respectively (Table 3). This limited exploration of model space suggests that the mean velocity between $Pr2$ and PmP is more likely in the
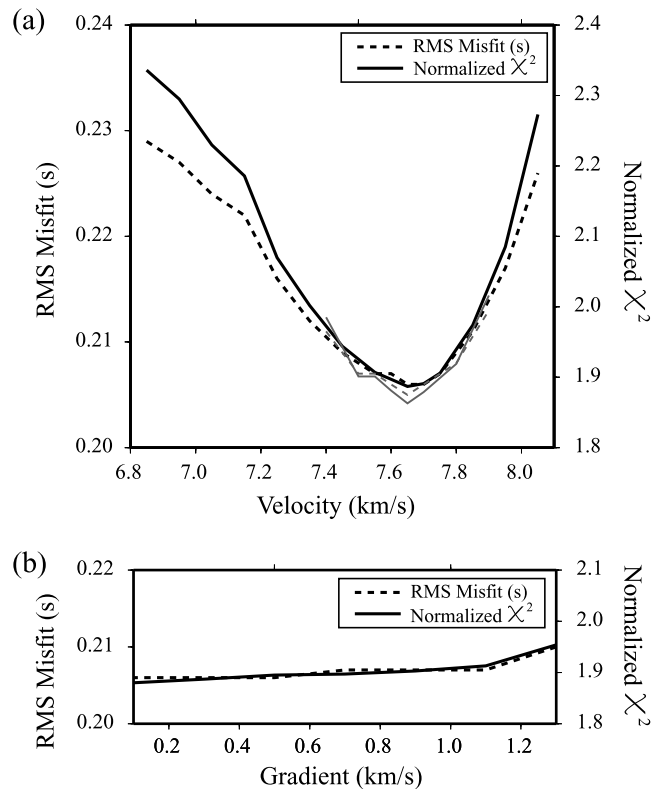

Figure 8. Analyses of uncertainty for the velocity and gradient of lower crustal layer 5. (a) RMS misfit and χ^2 of modeled $Pr2$ reflection travel times as a function of velocity at the upper boundary and the lower boundary of layer 5 (black continuous and dashed lines for a velocity gradient of 0.3 km s^{-1}, shaded continuous and dashed lines for no gradient). A velocity of $\sim$7.6–7.7 km s^{-1} minimizes the RMS misfit while allowing rays to be traced to a large number of observations. RMS misfit implies an uncertainty of $\pm$0.2 km s^{-1} in lower crustal velocities. (b) RMS misfit and χ^2 of modeled $Pr2$ reflection travel times as a function of velocity gradient with an average velocity of 7.65 km s^{-1}. The flat curve shows that the gradient is not well constrained.
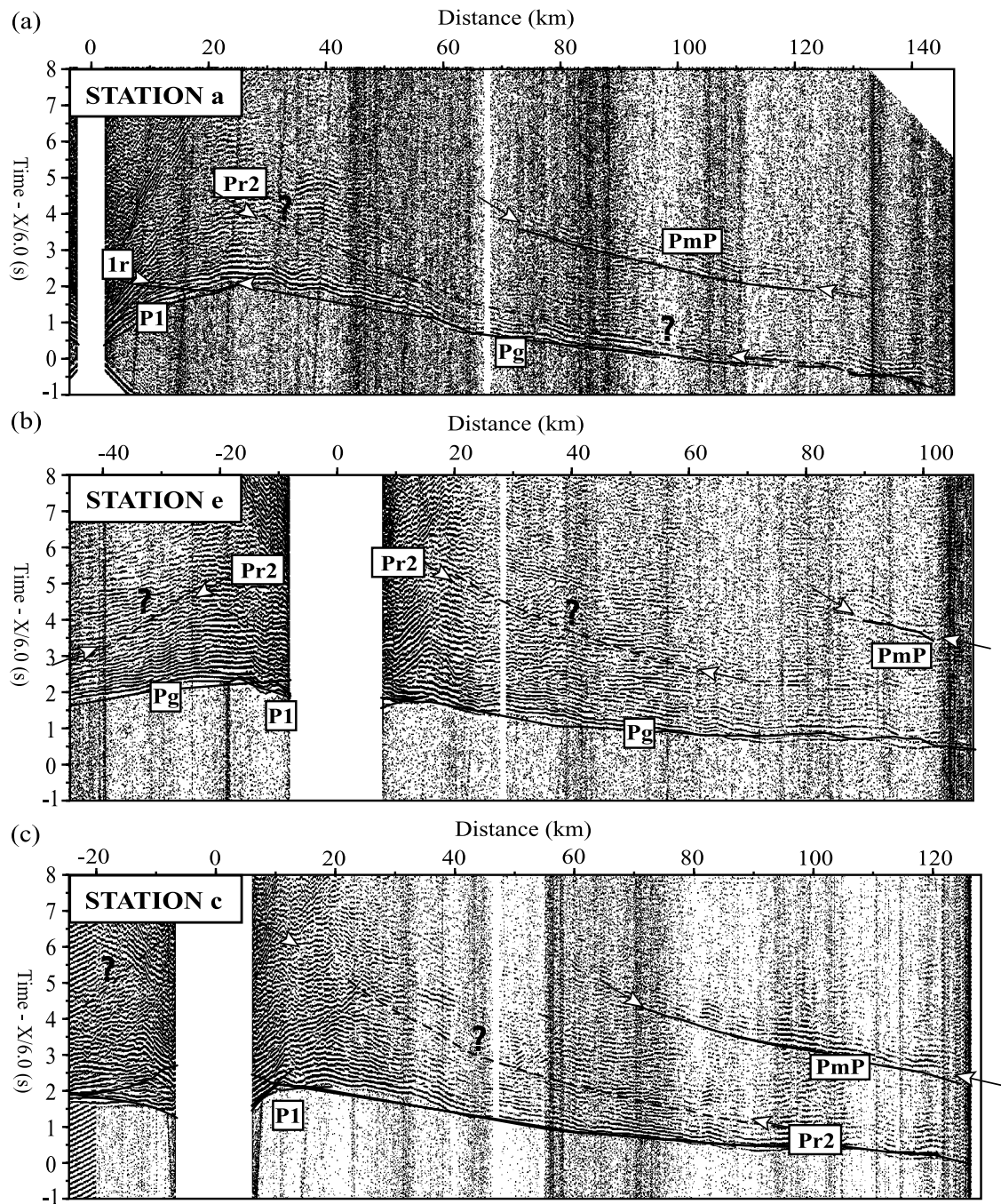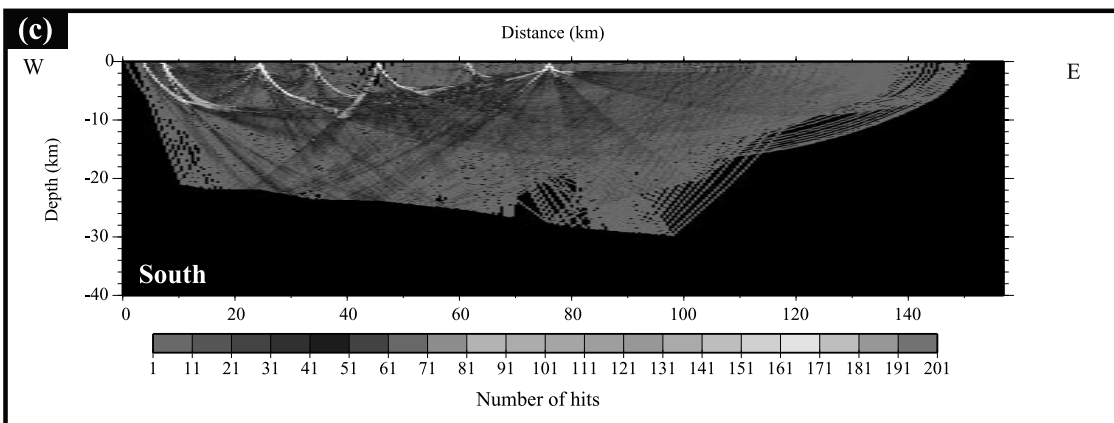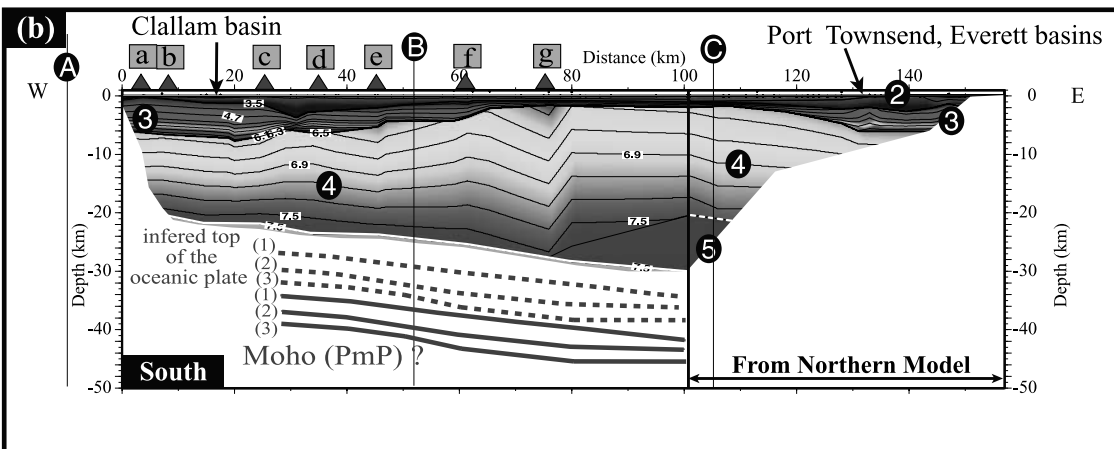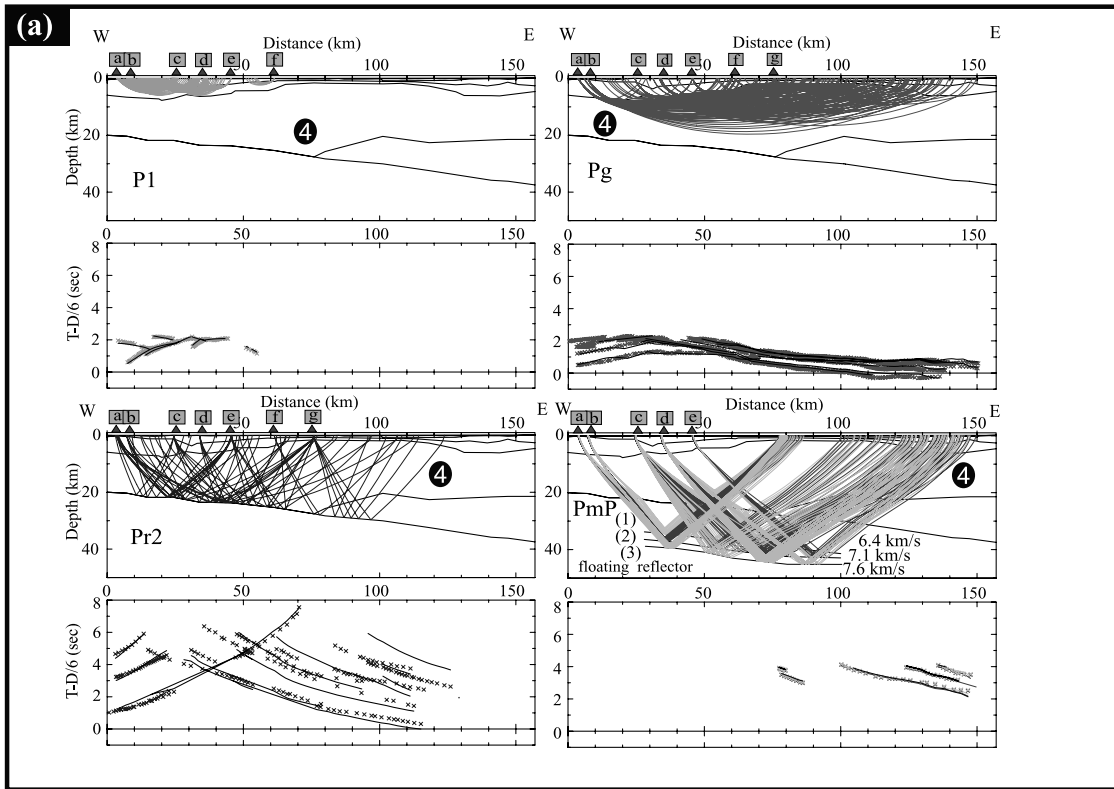
Figure 9. Record sections for wide-angle data (vertical component) for the southern Strait of Juan de Fuca. The refraction profiles are plotted with a reduction velocity of 6 km s^{-1} and a band-pass filter between 5 and 15 Hz, and amplitudes are scaled proportionally to the square root of offset. Labels indicate the different observed phases. Lines represent calculated travel times. (a) Station a. (b) Station e. (c) Station c.

Figure 10. (opposite) Southern velocity model. (a) Ray diagrams for the different modeled phases and the corresponding observed travel times for stations which record different arrivals. The black curves represent calculated travel times. The crosses represent the picked observed arrivals. Different colors correspond to different phases. (b) Velocity model across the southern Strait of Juan de Fuca. Triangles at the top of each velocity model indicate the positions of land recording stations. *Pr*2 refers to wide-angle deep reflectors. Solid circles with white numbers indicate layer numbers. Solid circles with white letters show the position of seismicity and gravity sections (A, B, C), perpendicular to the model and shown in Figures 12–14. For the southern model, Moho depths (green lines) are obtained by modeling of *PmP* arrival times, using a velocity between *Pr*2 and Moho of either 6.4 km s^{-1} (1), 7.1 km s^{-1} (2), or 7.6 km s^{-1} (3). The eastern part of the southern model, between ~100 and 158 km, is identical to the northern model. (c) Number of ray hits for the northern model which translates the ray coverage within the model. White color identifies a number of hits greater than 200. See color version of this figure at back of this issue.

range of 6.4–7.1 km s^{-1}, with a depth uncertainty at the Moho of ±1.5 km.

6. Comparison of Inferred Velocity Models With Three-Dimensional Tomography and Coincident MCS Data

[32] Our observations can be extended regionally by comparing the wide-angle velocity models with coincident multichannel reflection MCS lines 7 and 8 [*Tréhu et al.*, 2002] and with three-dimensional tomographic models determined from simultaneous inversion of SHIPS data and earthquake travel times [*Ramachandran*, 2001]. As the three-dimensional tomography depends only on direct or first-arrival travel times, the current study is able to provide complementary information since it includes secondary wide-angle reflected arrivals.

[33] The main features in common between MCS line 7 and Lithoprobe Vibroseis line 85-05 are the Leech River Fault (the boundary between Pacific Rim and Crescent-Siletz terranes) (Figure 2) and the "reflector band E" (Figure 11a). Reflector band E is observed as a series of prominent reflectors extending from 7 to 9.5 s two-way travel time (TWT). The E reflections have an apparent global dip toward the east. As was pointed out by *Tréhu et al.* [2002], SHIPS MCS line 7 shows only weak indications for reflection *F* or *O* [*Calvert and Clowes*, 1990; *Hyndman et al.*, 1990], interpreted as the top of oceanic crust or the oceanic Moho at around 10-s TWT and 10-km distance. We identify deeper reflections that we call "*G*" lying around 12 s (Figure 11a).

[34] The northern velocity model was converted to TWT for comparison with MCS line 7 (Figure 11a). No significant reflections are seen on the MCS data in the region of reflector *Pr*1. In the eastern Strait of Juan de Fuca, there is close agreement between the sedimentary basin imaged in the MCS line and the deepening of layers 2 and 3 from the refraction model over the distance range 100–160 km (Figure 5b). The base of the sediments inferred from the wide-angle data agrees well with the depth of the Port Townsend basin (a 4–5 km thickness of Tertiary sedimentary rocks [*Johnson and Mosher*, 2000]) determined from the three-dimensional tomography of *Brocher et al.* [2000] and *Ramachandran* [2001].

[35] An important result of our study is the close coincidence of *Pr*2 with the top of the E reflector band, particularly over the central half of the MCS line 7. We note that the amplitude of the *Pr*2 reflection is by far the strongest immediately east of stations 4 and 5 located at 65 and 80 km model distance, respectively (Figure 3). The reflection points for these strong arrivals occur over the model distance ranging from approximately 75 to 120 km and over the depth range from 26 to 32 km (Figure 5). The three-dimensional tomography model of *Ramachandran* [2001] shows an anomalous high-density body (7.6 km s^{-1}) just above the subducting slab at an equivalent location off the southeastern tip of Vancouver Island. The top of the body is at ∼26-km depth (∼8-s TWT). The feature is interpreted as an ultramafic body perhaps associated with Crescent Formation volcanic rocks. The strong *Pr*2 amplitudes are probably produced by large velocity contrasts near the top of this body.

[36] We compared our southern velocity model to SHIPS MCS line 8 (Figure 11b). There is close coincidence of the base of sediments inferred from the wide-angle data with the Clallam basin imaged on the MCS line between 0- and 60-km model distances in the west. With several kilometers of sedimentary rock thicknesses in the southern model, this contrasts with those in the western portion of the northern model, in which sediment cover over Crescent-Siletz terrane is very thin. Consistent with the wide-angle data, the E reflector band amplitude is weaker on MCS line 8 than on line 7, and its thickness seems smaller than in the north. However, as in the north, *Pr*2 generally appears to be associated with the deep reflectivity pattern. Modeling the *PmP* arrival times produces a Moho at about 12-s TWT (Figure 11b).

7. Comparison of the Wide-Angle Model With Seismicity

[37] The objectives of this comparison are (1) to relate the upper plate seismicity with the main geological features identified on the velocity model, (2) to identify the downgoing plate seismicity, and (3) to determine the relation between the top of this seismicity and the deeper structure of our wide-angle models, in particular the E reflector band and the *PmP* reflector.

[38] Seismicity presented on the sections of Figure 12 can be divided into two groups. Most of the seismicity appears to be concentrated in the upper crust, especially within Crescent-Siletz terrane. The deeper seismicity occurs within the downgoing plate. The top of the downgoing Juan de Fuca plate seismicity was estimated on the three sections. As there are only few events on section B between 0 and 80 km, the proposed limit of deeper seismicity has a large uncertainty and was plotted as a dashed line (Figure 12). The depths where the three sections intersected the northern and southern velocity models as well as the seismicity plotted along the velocity models were used to draw the possible top of downgoing plate seismicity along the two wide-angle velocity models (Figures 12d and 12e).

[39] On the southern model, modeling of *PmP* leads to a Moho which is between 5 and 7 km deeper than the estimated top of the downgoing plate seismicity (Figure 12). This thickness corresponds to the thickness of a normal oceanic crust [*White et al.*, 1992]. Thus significant portions of the intraplate seismicity appear to occur above the *PmP* within the subducting ocean crust. Furthermore, the inferred top of the downgoing plate appears to lie approximately 5–8 km deeper than reflector *Pr*2. On the northern model, the relation between *Pr*2 and the top of the seismicity is similar. The top of the Juan de Fuca plate seismicity increases in depth from 28 km in the west to 45 km in the east (Figure 12d).

[40] The E reflector band presents a notable low level of seismicity (Figure 12d). We converted the time thickness of the E reflector band on the MCS line 7 to depth using a velocity of 6.35 km s^{-1} as determined by *Cassidy and Ellis* [1991] from receiver function analysis. The base of the E reflector band (dashed gray line in Figure 12d) is very close to the top of the Juan de Fuca plate seismicity (solid dashed line in Figure 11d). The difference is never greater than 2 km, within the uncertainties of estimating the depths of both seismicity and velocity model interfaces; the agreement
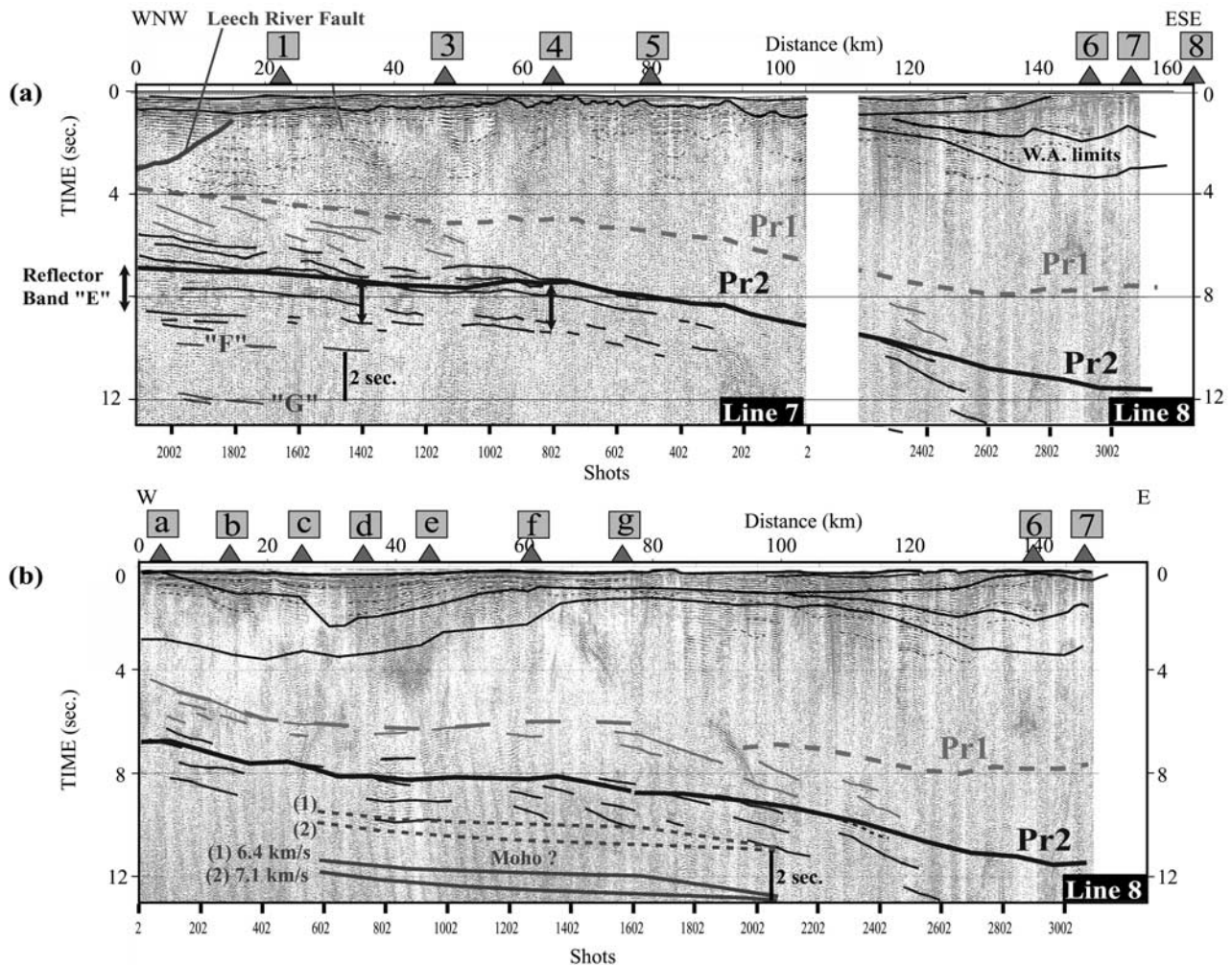
Figure 11. Stacked MCS record sections, after preliminary processing, along lines coincident with the wide-angle velocity models. The wide-angle velocity models are converted to time and superimposed on the MCS stacks. Eastern parts of northern and southern models are the same. $Pr1$ appears as a gray broken line, and $Pr2$ appears as a continuous black line. Thin continuous and broken lines are reflection horizons picked on the MCS record section. "G" refers to deep weak broken reflections around 11-s TWT. (a) SHIPS MCS line 7 coincident with northern model. (b) SHIPS MCS line 8 coincident with southern model. The Moho (shaded) reflection time is calculated from modeling of PmP arrival times.

would be even better if we used the higher velocity of 7.0–7.5 km s^{-1} inferred by *Ramachandran* [2001] for the region immediately above the downgoing ocean crust. Knowing the large uncertainty of seismicity location, we propose the hypothesis that additional underplating beneath the E reflector band appears unlikely since the top of the downgoing plate appears to coincide approximately with the base of the E reflectivity.

8. Gravity Modeling

8.1. Procedure

[41] Gravity modeling was undertaken to test the interpretation of the seismic structure data and to extend the structure over the entire Strait of Juan de Fuca. The results extend those of *Dehler and Clowes* [1992] and *Clowes et al.* [1997]. To build gravity models, the first constraint is provided by the surficial geology (Figure 2). In-depth

structure was first controlled by the geometry at the cross-line points with the southern and northern Strait of Juan de Fuca wide-angle models (Figures 5b and 10b). Densities were inferred using a variety of sources from wide-angle seismic velocities for sedimentary rock layers, layer 4 (Crescent-Siletz terrane), and high-velocity layer 5 (see Table 4). We used the appropriate velocity-density relation for the relevant types of rocks established by laboratory measurements [*Ludwig et al.*, 1970; *Nafe and Drake*, 1963; *Carlson and Raskin*, 1984; *Barton*, 1986]. In general, densities were consistent with previous gravity modeling in the area [*Dehler and Clowes*, 1992; *Clowes et al.*, 1997], modified slightly to fit the additional constraints provided by our seismic data. The water layer was assigned density of 1030 kg m^{-3}. The density of Crescent-Siletz formation deduced from the wide-angle velocity is 2930 kg m^{-3}. This value is at the high end of laboratory estimates for Crescent rocks reported by *Brocher and Christensen* [2001], but the
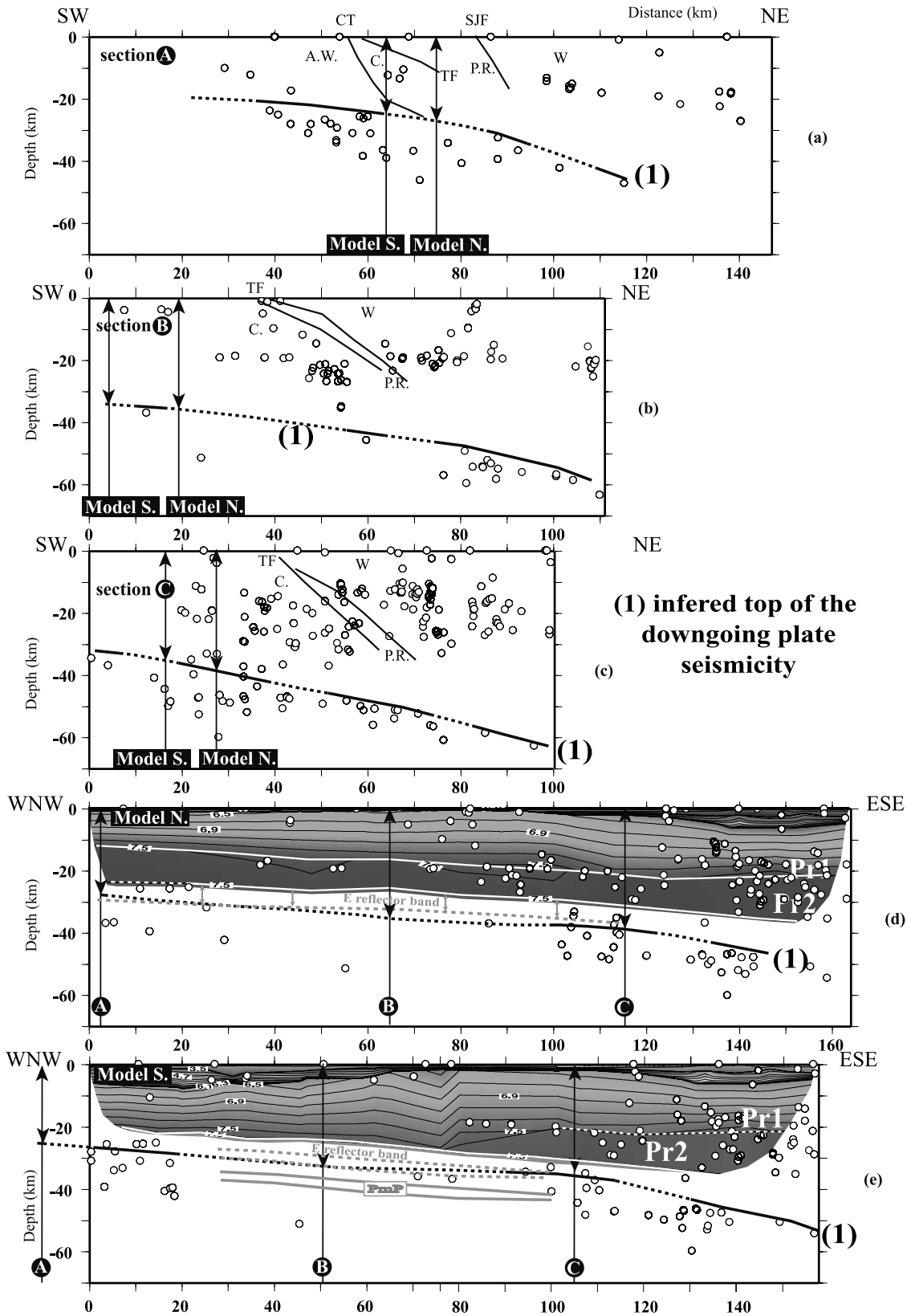
(1) infered top of the downgoing plate seismicity

Table 4. Density of Bodies

Body	Density, kg m^{-3}	Origin
	Model A	
Water	1030	
Sediments (layer 2)	2110	wide-angle
Upper crust (layer 3)	2580	wide-angle
Pacific Rim	2800	wide-angle [*Dehler and Clowes*, 1992; *Clowes et al.*, 1997]
Wrangellia	2900	*Dehler and Clowes* [1992]; *Clowes et al.* [1997]
Crescent Terrane (layer 4)	2930	wide-angle [*Brocher et al.*, 2001]
Accreted wedge	2600	*Dehler and Clowes* [1992]; *Clowes et al.* [1997]
High-density lower crust (Layer 5)	3030	wide-angle
E reflector band	2800	*Dehler and Clowes* [1992]; *Clowes et al.* [1997]
Mantle wedge	3290	*Dehler and Clowes* [1992]; *Clowes et al.* [1997]
Oceanic crust	2890	*Dehler and Clowes* [1992]; *Clowes et al.* [1997]; *Carlson and Raskin* [1984]
Oceanic mantle	3330	*Dehler and Clowes* [1992]; *Clowes et al.* [1997]
Mantle Ast.	3285	*Dehler and Clowes* [1992]; *Clowes et al.* [1997]
	Model B	
Water	1030	
Sediments east (layer 2)	2210	wide-angle
Sediments	2110	wide-angle
Upper crust (layer 3)	2520	wide-angle
Crescent Terrane (layer 4)	2930	wide-angle [*Brocher et al.*, 2001]
Accreted wedge	2600	*Dehler and Clowes* [1992]; *Clowes et al.* [1997]
Pacific Rim	2800	W.A. [*Dehler and Clowes*, 1992; *Clowes et al.*, 1997]
Wrangellia	2900	[*Dehler and Clowes*, 1992; *Clowes et al.*, 1997]
High-density lower crust (layer 5)	3030	wide-angle
E reflector band	2800	*Dehler and Clowes* [1992]; *Clowes et al.* [1997]
Oceanic crust	2890	*Dehler and Clowes* [1992]; *Clowes et al.* [1997]; *Carlson and Raskin* [1984]
Mantle wedge	3290	*Dehler and Clowes* [1992]; *Clowes et al.* [1997]
Oceanic mantle	3330	*Dehler and Clowes* [1992]; *Clowes et al.* [1997]
Mantle Ast.	3285	*Dehler and Clowes* [1992]; *Clowes et al.* [1997]

seismic model indicates that Crescent velocities and thus densities are higher at depth than in the upper few kilometers. The forearc upper mantle wedge density is 3290 kg m^{-3}. This value may be overestimated if the mantle wedge is serpentinized as has been recently proposed by *Brocher et al.* [2003] and *Blakely et al.* [2002]. The reference density used to compute gravity anomaly was 3000 kg m^{-3} as it represents a good central value of used densities. Models have been extended 400 km off the ends of the profiles.

[42] Lithoprobe and SHIPS crustal reflection lines also provide important constraints on the deep structure of the Insular Belt and Georgia Strait [*Clowes et al.*, 1987; *Calvert*, 1996; *Zelt et al.*, 2001] (Figure 13). Along section B (25–50 km), we based the structure on the interpretation of line 84-02 by *Clowes et al.* [1987] (Figure 14). At model distance 68 km, we also used results from receiver function analyses undertaken by *Cassidy* [1995; *Cassidy et al.*, 1998] to constrain the thickness of the crust and the position of the E reflector band. The thickness of the continental crust was set to 36–38 km throughout most of the Coast Belt, decreasing in the west to 33 km near the Insular Coast Belt contact [*Zelt et al.*, 1996; *Ramachandran*, 2001]. The position of the downgoing slab was deduced from the previous analysis of seismicity (Figure 12).

8.2. Modified Explanation for the Gravity High and Results

[43] The most prominent feature of the gravity data around Strait of Juan de Fuca (Figure 13) is the gravity high located on southeastern Vancouver Island (+65 mGal), corresponding roughly to the location where high-density igneous Crescent-Siletz terrane rocks crop out. The Coast Range Province, which is the southern equivalent of Crescent-Siletz formation, reaches a thickness of 30 km near its eastern edge. With a density of 2920 kg m^{-3}, it can explain the gravity high in western Washington [*Finn*, 1990]. A large thickness of Crescent-Siletz terrane may also contribute to the gravity high on southern Vancouver Island.

Figure 12. (opposite) Comparison of the 2D velocity model derived from wide-angle data with seismicity. Earthquakes were perpendicularly projected on each line from a distance of 25 km on either side. Labeled bold line indicates the inferred top of the downgoing plate seismicity. We used all the events from microearthquakes around the Strait of Juan de Fuca catalog compiled by *Mulder* [1995; also personal communication, 2001], with selected magnitude greater than 1 recorded between the years 1984 and 2000. (a) Seismicity along profile A (Figure 10). (b) Seismicity along profile B. (c) Seismicity along profile C. (d) Seismicity along northern model. Bold line indicates the top of the downgoing plate seismicity deduced from perpendicular sections A, B, and C. Dotted shaded line is the base of the "E reflector band," using a time thickness from MCS section 7 converted to depth with a velocity derived from receiver function analyses of *Cassidy* [1995]. (e) Seismicity along southern model. Bold line indicates the top of Juan de Fuca plate seismicity. CT, Crescent Thrust; SJF, San Juan Fault; TF, Tofino Fault; A.W., Accreted Wedge; C., Crescent; P.R., Pacific Rim; W, Wrangellia.
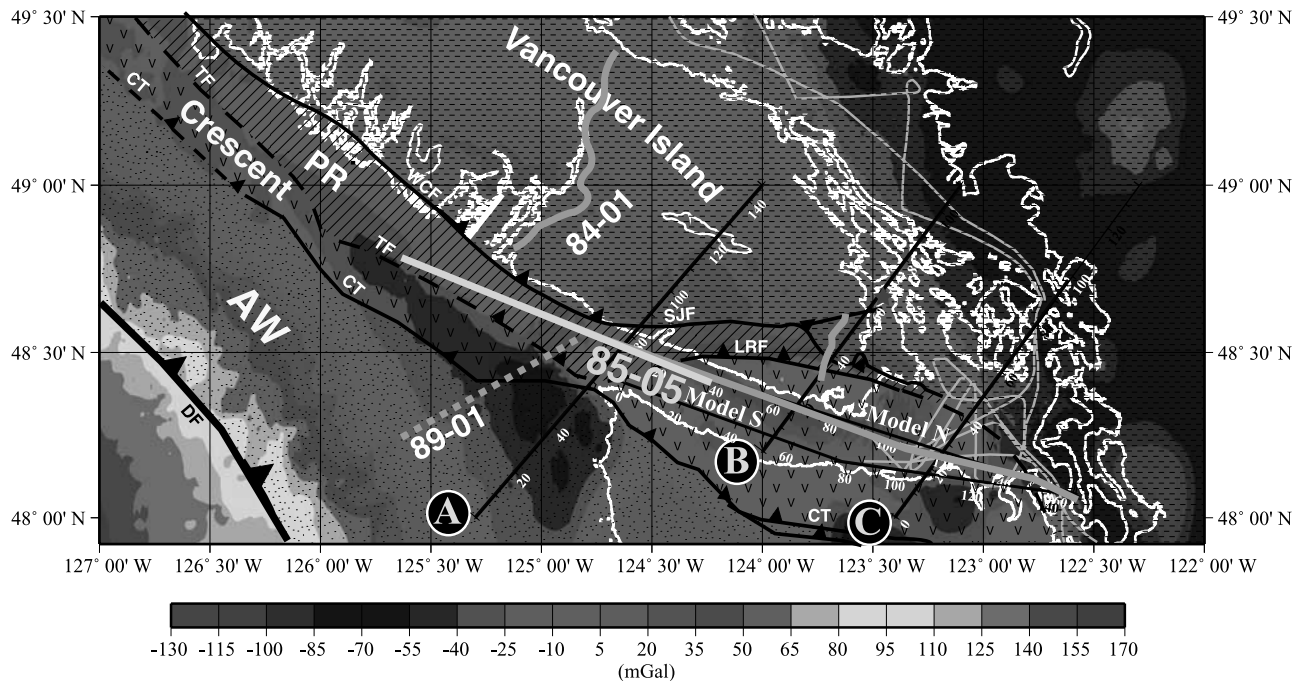
Figure 13. Gravity map of the Strait of Juan de Fuca. Data were interpolated to a grid with a grid size of 0.3 × 0.3 min. The three black lines (A, B, and C) indicate the location of modeled gravity profiles (A and B) (Figure 14) and three seismicity sections (A, B, and C) (Figure 12). Shaded lines show location of SHIPS line in Georgia Strait and eastern Juan de Fuca Strait. See color version of this figure at back of this issue.

[44] Recognizing the fundamental nonuniqueness of gravity interpretations, we adjusted the densities of the primary crustal elements (Crescent, high-density lower crust, E layer) within reasonable limits to determine the approximate sensitivity of the gravity model to density changes (Figure 14). A decrease in Crescent density to 2800 kg m^{-3} in general produces a local decrease of the central gravity anomaly by about ~15–30 mGal. Alternatively, an increase in density of the E layer to 3000 kg m^{-3}, nearly matching the high density of the lower crustal layer, produces an overall increase of about ~20 mGal. Characteristic of gravity modeling, there are many potential trade-offs in the crustal density distribution. Our density model represents a distribution that is as consistent as possible with the seismic velocity constraints. Although we crudely attempt to account for three-dimensional variations with multiple two-dimensional models, we nevertheless recognize that unknown three-dimensional effects may be present and careful three-dimensional modeling is required.

[45] Our modeling shows that the gravity high may be consistent with (1) a large thickness of Crescent-Siletz terrane beneath the Strait of Juan de Fuca and (2) high-velocity and high-density rocks within the lower crust, and (3) shallow depth of the subducting ocean crust and mantle beneath the Olympic Peninsula and southern Vancouver Island. Together, these features produce a large positive anomaly in southern Vancouver Island and the northern Strait of Juan de Fuca (Figures 13 and 14). A previous interpretation of this anomaly by *Dehler and Clowes* [1992] assumed that the Crescent-Siletz terrane was less than 7 km in thickness. They assumed that the lower 5 km of this unit had a density of 3200 kg m^{-3}, which may represent high-

density lower crust but is more readily associated with upper mantle material. Our model (Figure 14b) contrasts with this previous result in that Crescent-Siletz terrane has a more normal lower crustal density (2930 kg m^{-3}), but it is much thicker and extends to nearly 20 km depth, below which occurs a 5–10 km thick layer of possible mantle material. Our modeling shows also that the top of the downgoing slab, lying just beneath the E reflector band in agreement with seismicity, is consistent with observed long wavelength, lower density gravity. In the western Strait of Juan de Fuca, the gravity model is consistent with accreted wedge sediments above the downgoing plate (Figure 14). Both southwestern and eastern Strait of Juan de Fuca sediment basins are included in the gravity models. Contrasting sediment thicknesses between north and south are consistent with observed gravity data.

9. Discussion and Results

9.1. Crescent-Siletz Terrane

[46] Beneath the sedimentary rocks the upper crust is mainly composed of Crescent-Siletz terrane tholeiitic basalts (layer 4). *Pg* compressional velocities range from 6.2 (±0.1) to 7.5 (±0.1) km s^{-1}, consistent with basalts [*Christensen*, 1996]. Furthermore, we have forward modeled the shear wave phase *Sg* and calculated a Poisson's ratio σ of 0.25 ± 0.3 (Figures 3 and 5). Based on published Poisson ratios for different rock lithologies [*Christensen*, 1996] this value is less than σ for a typical basalt (0.29). A possible explanation of the lowered values is metamorphism of the basalt to greenschist facies for which *Christensen* [1996] quotes a σ of 0.26. The minimum thickness of
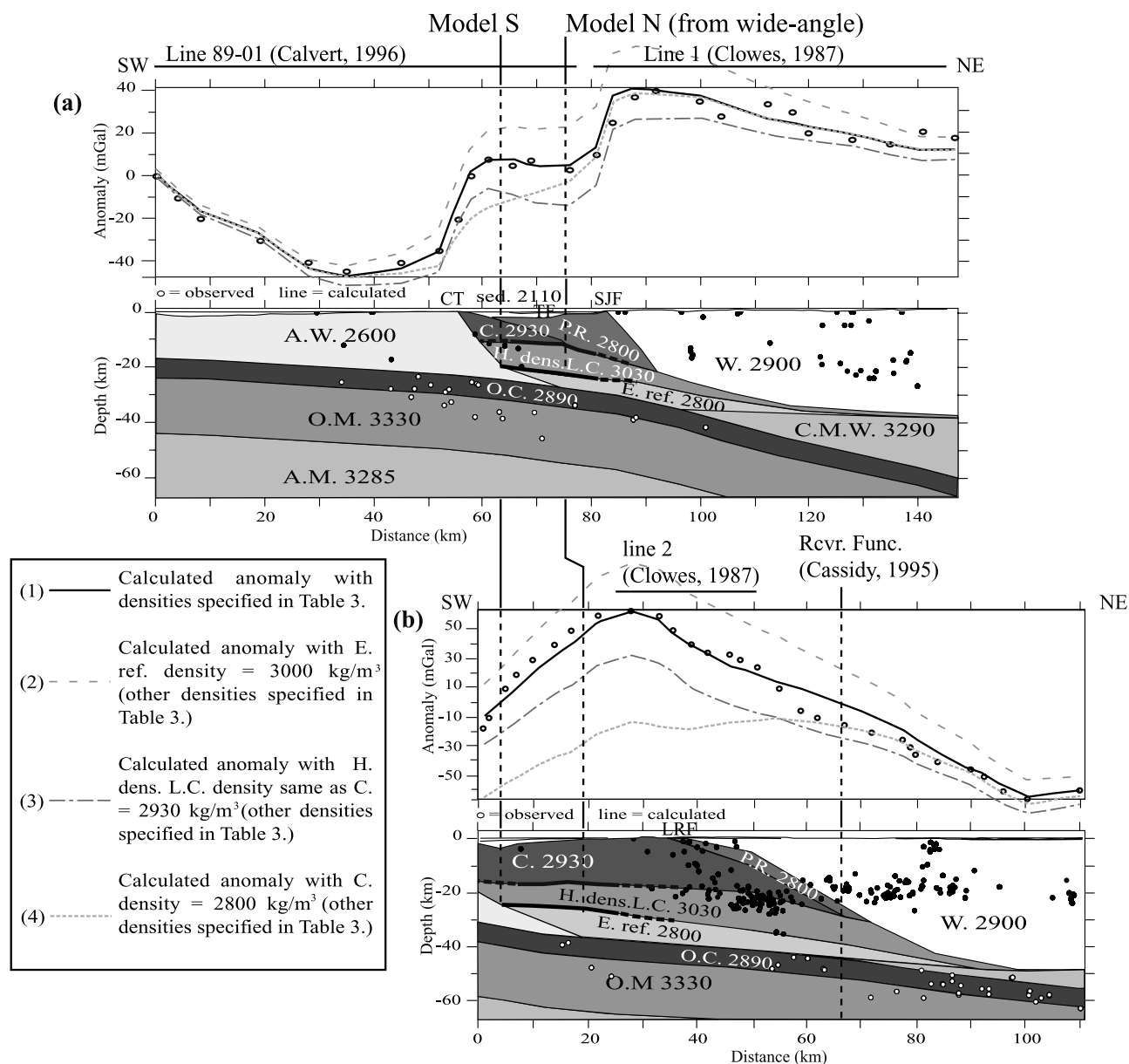
Figure 14. Gravity models across the Strait of Juan de Fuca (for location see Figure 13). Densities were deduced from wide-angle velocities for constrained layers. Other densities are consistent with that in the work of *Clowes et al.* [1997], *Dehler and Clowes* [1992], and *Finn* [1990]. Some constraints were obtained from MCS Lithoprobe lines and receiver function analyses [*Cassidy*, 1995]. Heavy, dark shaded line symbolizes Pr1, and heavy black one symbolizes Pr2. Calculated anomalies have desegregated in three steps showing the effect of high-density lower crust, Crescent, and E reflector band. (a) Gravity model along line A in the western Strait of Juan de Fuca. (b) Gravity model along line B in the central Strait of Juan de Fuca. sed., sediments; A.W., accreted wedge; C., Crescent terrane; P.R., Pacific Rim; H. dens. L.C., high-density lower crust; E. ref., E reflector band; O.C., oceanic crust, W., Wrangellia; C.M.W., continental mantle wedge; O.M., oceanic mantle; and A.M., asthenospheric mantle.

Crescent-Siletz terrane (12 km in the west and 22 km in the east) was established from the maximum depth extent of *Pg* turning rays and from the additional weak constraint of a possible reflector *Pr*1 at the base of the Crescent-Siletz terrane. South of the study area, Paleocene and Eocene age accreted oceanic terrane (Siletzia) is comparable or greater in thickness, reaching 25–35 km beneath the Oregon Coast Range [*Tréhu et al.*, 1994]. Crescent-Siletz terrane clearly extends north of the Strait of Juan de Fuca, along the margin, as identified by a strong magnetic anomaly and by petroleum exploration drill hole sampling [e.g., *Hyndman et al.*, 1990]. From multichannel line 85-05 and several other MCS lines perpendicular to the continental margin (e.g., 85-01, 89-01, 84-02), the thickness of Crescent-Siletz terrane off Vancouver Island was previously interpreted as only 6 km [*Hyndman et al.*, 1990; *Calvert*,

1996], typical of normal oceanic crust. However, a large thickness for Crescent-Siletz in the south Vancouver Island region is consistent with recent results from simultaneous inversion of earthquake and SHIPS controlled-source data [*Ramachandran*, 2001], which suggest that a thicker Crescent-Siletz terrane extends farther north than the mouth of Strait of Juan de Fuca.

9.2. Lower Crustal Structure

[47] The lower crustal structure has been determined by mapping the reflector *Pr*2. On the northern section, it lies at a depth of 23 km in the west and 35 km in the east (Figure 5b). Velocities of $7.5–7.7$ km s^{-1} in layer 5 between *Pr*1 and *Pr*2, with an average velocity of 7.6 km s^{-1} (Figure 8), are best constrained in the central part of the model. On the coincident MCS reflection line 7, this zone generally has low reflectivity (Figure 11a). An equivalent feature with a velocity of 7.7 km s^{-1} at depth ranging from 20 to 25 km was previously identified beneath southern Vancouver Island above the downgoing crust [*Spence et al.*, 1985; *Drew and Clowes*, 1990]. *Ramachandran* [2001] also found high-velocity zones beneath the Crescent-Siletz terrane. Furthermore, his three-dimensional velocity models showed that they were generally localized to three regions, including a portion of the Strait of Juan de Fuca, consistent with the present study, and the area beneath southern Vancouver Island to the northwest studied by *Spence et al.* [1985]. Such high velocities of $7.6 ± 0.2$ km s^{-1} are inconsistent with a basaltic or gabbroic composition. Having only a weak to no-velocity contrast relative to the Crescent-Siletz terrane, layer 5 is preferably interpreted as a deeper component of Crescent-Siletz, perhaps a thin discontinuous slice of an ultramafic mantle layer that was partially serpentinized or otherwise metamorphosed [*Chian and Louden*, 1994; *Chian et al.*, 1995; *Godfrey et al.*, 1997]. As suggested by *Ramachandran* [2001], the ultramafic layer could be related to the deep mantle source region that produced Crescent-Siletz terrane. Alternatively, layer 5 could have been accreted in a separate event or events as described by *Green et al.* [1986] and *Clowes et al.* [1987], a whole underplated slab or remnant of subducted lithosphere perhaps detached when the subduction zone jumped westward to its recent position or an imbricated package of mafic rocks derived by continuous accretion from the top of the subducting oceanic crust.

[48] Reflector *Pr*2 is weaker and less continuous in the southern strait (Figure 10b). However, no evidence at all is seen for reflector *Pr*1 in the southern strait. Thus high-velocity lower crust or upper mantle material (layer 5), which is evident in the northern model, may be absent in the southern model, and Crescent-Siletz terrane could extend down to reflector *Pr*2. The Crescent-Siletz terrane, with or without its associated ultramafics, may thus reach a thickness of 20 km in southwestern Strait of Juan de Fuca and almost 35 km in the southeast. A similar large thickness for Crescent-Siletz terrane was obtained by *Ramachandran* [2001] from seismic tomography of SHIPS data on southern Vancouver Island.

9.3. E-Reflector Band

[49] The E region of MCS reflectivity is regionally extensive [*Clowes et al.*, 1987] and electrically conductive

[*Kurtz et al.*, 1986, 1990]. It has a pronounced lower density $\rho = 2800$ kg m^{-3}, a low velocity for *S* waves [*Cassidy et al.*, 1998], and a high Poisson's ratio ($0.27–0.38$) [*Cassidy*, 1995]. These attributes support an E zone dominated by thin, fluid-saturated cracks [*Cassidy and Ellis*, 1991]. There have been two main hypotheses for the origin of the E layer. The first is structural, proposing that the E layer is linked to major faults within the accretionary wedge [*Calvert and Clowes*, 1990; *Calvert*, 1996] and truncates at depth a major terrane boundary mapped near the surface. The second hypothesis is that reflectors are caused by fluid-filled porosity created by dehydration reactions associated with changes in metamorphic facies and contrasting physical properties [*Hyndman*, 1988; *Kurtz et al.*, 1990].

[50] The combined wide-angle seismic, MCS, and seismicity results in the present study contribute to our understanding of the origin of the E layer. The primary results are that (1) reflector *Pr*2 is generally associated with the top of the E reflector band (Figures 11 and 12) and (2) the E layer lies just above the top of the subducting oceanic crust as inferred from *PmP* in the southern Strait of Juan de Fuca and from the distribution of Benioff zone seismicity (Figures 12 and 10b). Furthermore, we note that there are apparently no low velocities observed in this region consistent with sheared accretionary sediments, either in the present study or in the study of *Ramachandran* [2001], within the resolution of the measurements. However, at E-layer depths (>20 km), such sediments may be metamorphosed and their velocities increased. Metamorphic rocks as the origin of E-layer reflectivity cannot be excluded. Alternatively, the E-layer reflectivity may be due to layered, altered serpentinized mafics and ultramafics, perhaps intensely sheared as they are stripped from the downgoing plate and underplated. Located just above the decollement, this sheared zone may provide increased permeability that is filled with fluids under high pressure expelled from the downgoing plate.

9.4. Subducting Juan de Fuca Plate

[51] The depths of the oceanic Moho are $35 ± 1.5$ km beneath the western strait and $42 ± 1.5$ km beneath the eastern strait (Figure 10b). These results are comparable to those of *Tréhu et al.* [2002] who modeled a Moho at $34–36$ km depth beneath western Strait of Juan de Fuca dipping $7°$ to the east-southeast and at 46 km beneath the eastern Olympic Peninsula. For either of the mean velocities proposed, the Juan de Fuca plate seismicity falls mainly within the oceanic crust (Figures 12d and 12e).

[52] On northern MCS line 7 (Figure 11a), a weak reflector (*G*) occurs beneath the westernmost portion of the line at a depth of 12-s TWT. Since this occurs about 2 s or 6 km beneath the top of the downgoing plate seismicity, we interpret the *G* reflector as the oceanic Moho (Figure 9), i.e., *PmP* in wide-angle data. On Lithoprobe MCS line 84-01, a short reflector (*F*) was observed at 10-s TWT beneath western Vancouver Island. With more continuous observations of oceanic crust farther seaward on GSC line 85-01, reflector *F* was interpreted as the top of the subducting oceanic crust [*Hyndman et al.*, 1990; *Calvert*, 1996]. This interpretation is consistent with the present modeling of the

new SHIPS seismic data and with the modeling of *Tréhu et al.* [2002].

10. Conclusions

[53] SHIPS wide-angle seismic data and gravity modeling along the Strait of Juan de Fuca show that the Eocene volcanic Crescent-Siletz terrane, which outcrops on southern Vancouver Island, is much thicker in this region than previously interpreted. Beneath the northern strait, a weak reflector deepens eastward from 12- to 22-km depth and may separate Crescent-Siletz terrane from an associated localized mantle root. A deeper, much stronger reflector, dipping eastward from 23- to 36-km depth, correlates with the top of reflector band E, most likely a shear zone or underplated material of alternating mafic/ultramafic layers. A high-velocity zone between the two reflectors, well constrained at 7.6 ± 0.2 km s^{-1}, may represent a local lower crustal unit of ultramafic mantle, which could be either underplated mantle material or the lowermost part of a very thick Crescent-Siletz terrane. Beneath the southern strait, the E reflector band and the wide-angle midcrustal reflectors are less well defined. However, a strong wide-angle reflector dipping east from 35 ($\pm$1.5)- to 42 ($\pm$1.5)-km depth may be interpreted as the Moho of the subducting ocean crust. Seismicity within the Juan de Fuca plate lies mainly above the subducting Moho and thus within the subducting oceanic crust.

References

Atwater, B. F., Evidence for great Holocene earthquakes along the outer coast of Washington State, *Science*, *236*, 942–944, 1987.

Atwater, B. F., Geological evidence for earthquakes during the past 2000 years along the Copalis River, southern coastal Washington, *J. Geophys. Res.*, *97*, 1901–1919, 1992.

Babcock, R. S., R. F. Burmester, D. C. Engebretson, A. Warnock, and K. P. Clark, A rifted margin origin for the crescent basalts and related rocks in the northern Coast Range volcanic province, Washington and British Columbia, *J. Geophys. Res.*, *97*, 6799–6821, 1992.

Barton, P. J., The relationship between seismic velocity and density in the continental crust—A useful constraint?, *Geophys. J. R. Astron. Soc.*, *87*, 195–208, 1986.

Blakely, R. J., T. M. Brocher, and R. E. Wells, Cascadia gravity and magnetic anomalies delineate hydrated forearc mantle, *EOS Trans. AGU*, *83*(47), Fall Meet. Suppl., Abstract S21C-04, 2002.

Brandon, M. T., Origin of igneous rocks associated with melanges of the Pacific rim complex, western Vancouver Island, Canada, *Tectonics*, *8*, 1115–1136, 1989.

Brandon, M. T., and A. R. Calderwood, High-pressure metamorphism and uplift of the Olympic subduction complex, *Geology*, *18*, 1252–1255, 1990.

Brocher, T. M., and N. I. Christensen, Density and velocity relationships for digital sonic and density logs from coastal Washington and laboratory measurements of Olympic Peninsula mafic rocks and greywackes, *U. S. Geol. Surv. Open File Rep.*, *01-264*, 29 pp., 2001.

Brocher, T. M., et al., Wide-angle seismic recordings from the 1998 seismic hazards investigation of Puget Sound (SHIPS), western Washington and British Columbia, U.S. Department of the Interior, *U.S. Geol. Surv. Open File Rep.*, *99-314*, 123 pp., 1999.

Brocher, T. M., T. Parsons, M. A. Fisher, A. M. Tréhu, G. D. Spence, and the SHIPS Working Group, Three-dimensional tomography in the eastern Strait of Juan de Fuca: Preliminary results from SHIPS, the 1998 Seismic Hazards Investigation in Puget Sound, in *Neotectonics of the Eeastern Juan de Fuca Strait: A Digital Geological and Geophysical Atlas* [CD-ROM], edited by D. C. Mosher and S. Y. Johnson, *Geol. Surv. Can. Open File Rep.*, *3931*, 2000.

Brocher, T. M., T. Parsons, R. J. Blakely, N. I. Christensen, M. A. Fisher, R. E. Wells, and the SHIPS Working Group, Upper crustal structure in Puget Lowland, Washington: Results from the 1998 Seismic Hazards Investigation in Puget Sound, *J. Geophys. Res.*, *106*, 13,541–13,564, 2001.

Brocher, T. M., T. Parsons, A. M. Tréhu, C. M. Snelson, and M. A. Fisher, Seismic evidence for widespread serpentinized forearc upper mantle along the Cascadia margin, *Geology*, *31*, 267–270, 2003.

Calvert, A. J., Seismic reflection constraints on imbrication and underplating of the northern Cascadia convergent margin, *Can. J. Earth Sci.*, *33*, 1294–1307, 1996.

Calvert, A. J., and R. M. Clowes, Deep, high-amplitude reflections from a major shear zone above the subducting Juan de Fuca plate, *Geology*, *18*, 1091–1094, 1990.

Calvert, A. J., and R. M. Clowes, Seismic evidence for the migration of fluids within the accretionary complex of western Canada, *Can. J. Earth Sci.*, *28*, 542–556, 1991.

Carlson, R. L., and G. S. Raskin, Density of the ocean crust, *Nature*, *311*, 555–558, 1984.

Cassidy, J. F., A comparison of the receiver structure beneath stations of the Canadian National Seismograph Network, *Can. J. Earth Sci.*, *32*, 938–951, 1995.

Cassidy, J. F., and R. M. Ellis, Shear wave constraints on a deep crustal reflective zone beneath Vancouver Island, *J. Geophys. Res.*, *96*, 19,843–19,851, 1991.

Cassidy, J. F., R. M. Ellis, C. Karavas, and G. C. Rogers, The northern limit of the subducted Juan de Fuca plate system, *J. Geophys. Res.*, *103*, 26,949–26,961, 1998.

Cerveny, V., I. Molotkov, and I. Psencik, *Ray Method in Seismology*, Charles Univ. Press, Prague, 1977.

Chian, D., and K. E. Louden, The continent-ocean transition across the southwest Greenland margin, *J. Geophys. Res.*, *99*, 9117–9135, 1994.

Chian, D., K. E. Louden, and I. Reid, Crustal structure of the Labrador Sea conjugate margin and implications for the formation of nonvolcanic continental margins, *J. Geophys. Res.*, *100*, 24,239–24,253, 1995.

Christensen, N. I., Poisson's ratio and crustal seismology, *J. Geophys. Res.*, *101*, 3139–3156, 1996.

Clowes, R. M., M. T. Brandon, A. G. Green, C. J. Yorath, A. Sutherland Brown, E. R. Kanasewich, and C. Spencer, LITHOPROBE—Southern Vancouver Island: Cenozoic subduction complex imaged by deep seismic reflections, *Can. J. Earth Sci.*, *24*, 31–51, 1987.

Clowes, R. M., D. J. Baird, and S. A. Dehler, Crustal structure of the Cascadia subduction zone, southwestern British Columbia, from potential field and seismic studies, *Can. J. Earth Sci.*, *34*, 317–335, 1997.

Dehler, S. A., and R. M. Clowes, Integrated geophysical modelling of terranes and other structural features along the western Canadian margin, *Can. J. Earth Sci.*, *29*, 1492–1508, 1992.

DeMets, C., R. G. Gordon, D. F. Argus, and S. Stein, Current plate motions, *Geophys. J. Int.*, *101*, 425–478, 1990.

Dewey, J. W., D. P. Hill, W. L. Ellsworth, and E. R. Engdahl, Earthquakes, faults and the seismotectonic framework of the contiguous United States, in *Geophysical Framework of the Continental United States*, edited by L. C. Pakiser and W. D. Mooney, *Mem. Geol. Soc. Am.*, *172*, 541–576, 1989.

Drew, J., and R. M. Clowes, A re-interpretation of the seismic structure across the active subduction zone of western Canada—CCSS Workshop Topic I, onshore-offshore data set, in *Structures of Laterally Heterogeneous Structures Using Seismic Refraction and Reflection Data*, edited by A. G. Green, *Pap. Geol. Surv. Can.*, *89-13*, 115–132, 1990.

Duncan, R. A., A captured island chain in the Coast Range of Oregon and Washington, *J. Geophys. Res.*, *87*, 10,827–10,837, 1982.

Engebretson, D. C., K. P. Kelley, H. J. Cashman, and M. Richards, 180 million years of subduction, *GSA Today*, *2*, 94–95, 1992.

Finn, C., Geophysical constraints on Washington convergent margin structure, *J. Geophys. Res.*, *95*, 19,533–19,546, 1990.

Fisher, M. A., et al., Seismic survey probes urban earthquake hazards in Pacific Northwest, *EOS Trans. AGU*, *80*(2), 13, 16–17, 1999.

Flueh, E. R., et al., New seismic images of the Cascadia subduction zone from cruise SO108-ORWELL, *Tectonophysics*, *293*, 69–84, 1998.

Fuis, G. S., West margin of North America—A synthesis of recent seismic transects, *Tectonophysics*, *288*, 265–292, 1998.

Gerdom, M., A. M. Tréhu, E. R. Flueh, and D. Klaeschen, The continental margin off Oregon from seismic investigations, *Tectonophysics*, *329*, 79–97, 2001.

Glassey, W., Geochemistry and tectonics of the Crescent volcanic rocks, Olympic Peninsula, Washington, *Geol. Soc. Am. Bull.*, *85*, 785–794, 1974.

Godfrey, N. J., B. C. Beaudoin, S. L. Klemperer, and the Mendocino Working Group USA, Ophiolitic basement to the Great Valley forearc basin, California, from seismic and gravity data: Implications for crustal growth at the North American continental margin, *Geol. Soc. Am. Bull.*, *109*, 1536–1562, 1997.

Goldfinger, C., H. Nelson, and J. E. Johnson, Holocene recurrence of Cascadia great earthquakes based on turbidite event record, *EOS Trans. AGU*, *80*(46), Fall Meet. Suppl., F1024, 1999.

Green, A. G., R. M. Clowes, C. J. Yorath, C. Spencer, E. R. Kanasewich, M. T. Brandon, and A. Sutherland Brown, Seismic reflection imaging of the subducting Juan de Fuca plate, *Nature*, *319*, 210–213, 1986.

Heaton, T. H., and S. H. Hartzell, Earthquake hazards on the Cascadia Subduction Zone, *Science*, *236*, 162–168, 1987.

Holbrook, W. S., E. C. Reiter, G. M. Purdy, D. Sawyer, P. L. Stoffa, J. A. Austin Jr., J. Oh, and J. Makris, Deep structure of the U.S. Atlantic continental margin, offshore South Carolina, from coincident ocean bottom and multichannel seismic data, *J. Geophys. Res.*, *99*, 9155–9178, 1994.

Hyndman, R. D., Dipping seismic reflectors, electrically conductive zones, and trapped water in the crust over a subducting plate, *J. Geophys. Res.*, *93*, 13,391–13,405, 1988.

Hyndman, R. D., Giant earthquakes of the Pacific Northwest, *Sci. Am.*, *273*, 50–57, 1995a.

Hyndman, R. D., The lithoprobe corridor across the Vancouver Island continental margin: The structural and tectonic consequences of subduction, *Can. J. Earth Sci.*, *32*, 1777–1802, 1995b.

Hyndman, R. D., C. J. Yorath, R. M. Clowes, and E. E. Davis, The northern Cascadia subduction zone at Vancouver Island: Seismic structure and tectonic history, *Can. J. Earth Sci.*, *27*, 313–329, 1990.

Johnson, S. Y., and D. C. Mosher, The eastern Juan de Fuca Strait—Regional geology map, in *Neotectonics of the Eastern Juan de Fuca Strait: A Digital Geological and Geophysical Atlas* [CD-ROM], edited by D. C. Mosher and S. Y. Johnson, *Geol. Surv. Can. Open File Rep.*, *3931*, 2000.

Journeay, J. M., and R. M. Friedman, The coast belt thrust system: Evidence of Late Cretaceous shortening in southwest British Columbia, *Tectonics*, *12*, 756–775, 1993.

Kanamori, H., and T. H. Heaton, The wake of a legendary earthquake, *Nature*, *379*, 203–204, 1996.

Khazaradze, G., A. Qamar, and H. Dragert, Tectonic deformation in western Washington from continuous GPS measurements, *Geophys. Res. Lett.*, *26*, 3153–3156, 1999.

Kurtz, R. D., J. M. Delaurier, and J. C. Gupta, A magnetotelluric sounding across Vancouver Island detects the subducting Juan de Fuca plate, *Nature*, *321*, 596–599, 1986.

Kurtz, R. D., J. M. DeLaurier, and J. C. Gupta, The electrical conductivity distribution beneath Vancouver Island: A region of active plate subduction, *J. Geophys. Res.*, *95*, 10,929–10,946, 1990.

Ludwig, W. J., J. E. Nafe, and C. L. Drake, Seismic refraction, in *The Sea: Ideas and Observations on Progress in the Study of the Seas*, edited by A. E. Maxwell, Wiley-Interscience, New York, 1970.

Ludwin, R., C. S. Weaver, and R. S. Crosson, Seismicity of the Pacific Northwest, in *Neotectonics of North America, Decade of North American Geology*, vol. GSMV-1, edited by D. B. Slemmons, M. D. Zoback, and D. D. Balckwell, pp. 77–88, Geol. Soc. of Am., Boulder, Colo., 1991.

Malone, S., R. S. Crosson, K. C. Creager, A. Qamar, G. C. Thomas, R. Ludwin, K. G. Troost, D. B. Booth, and R. A. Haugerud, Preliminary report on the $M_w = 6.8$ Nisqually, Washington earthquake of 28 February 2001, *Seismol. Res. Lett.*, *72*, 353–362, 2001.

Massey, N. W. D., Metchosin igneous complex, southern Vancouver Island: Ophiolite stratigraphy developed in an emergent island setting, *Geology*, *14*, 602–605, 1986.

Mazzotti, S., H. Dragert, R. D. Hyndman, M. Miller, and J. Henton, GPS deformation in a region of high crustal seismicity: N. Cascadia forearc, *Earth Planet. Sci. Lett*, *198*, 41–48, 2002.

Miller, K. C., G. R. Keller, J. M. Gridley, J. H. Luetgert, W. D. Mooney, and H. Thybo, Crustal structure along the west flank of the Cascades, western Washington, *J. Geophys. Res.*, *102*, 17,857–17,873, 1997.

Mulder, T. L., Small earthquakes in southwestern British Columbia, M. S. thesis, Univ. of Victoria, B. C., Canada, 1995.

Nafe, J., and C. Drake, Physical properties of marine sediments, in *The Sea*, edited by M. N. Hill, pp. 794–828, Wiley-Interscience, New York, 1963.

Nedimovic, M. R., R. D. Hyndman, K. Ramachandran, and G. D. Spence, Reflection signature of seismic and aseismic slip on the northern Cascadia subduction interface, *Nature*, *424*, 416–420, 2003.

Parsons, T., A. M. Tréhu, J. H. Luetgert, K. Miller, F. Kilbride, R. E. Wells, M. A. Fisher, E. Flueh, U. S. ten Brink, and N. I. Christensen, A new view into the Cascadia Subduction Zone and volcanic arc: Implications for earthquake hazards along the Washington margin, *Geology*, *26*, 199–202, 1998.

Parsons, T., R. E. Wells, M. A. Fisher, E. Flueh, and U. S. ten Brink, Three-dimensional velocity structure of Siletzia and other accreted terranes in the Cascadia forearc of Washington, *J. Geophys. Res.*, *104*, 18,015–18,039, 1999.

Ramachandran, K., Velocity structure of south west British Columbia and north west Washington, from 3-D non-linear seismic tomography, Ph.D. thesis, 198 pp., Univ. of Victoria, B. C., Canada, 2001.

Riddihough, R. P., One hundred million years of plate tectonics in western Canada, *Geosci. Can.*, *9*, 28–34, 1982.

Riddihough, R. P., and R. D. Hyndman, The modern plate tectonic regime of the continental margin of western Canada, in *Geology of the Cordilleran Orogen in Canada*, edited by H. Gabrielse and C. J. Yorath, pp. 435–455, Geol. Surv. of Can., Ottawa, 1991.

Rogers, G. C., An assessment of the megathrust earthquake potential of the Cascadia subduction zone, *Can. J. Earth Sci.*, *25*, 844–852, 1988.

Saltus, R. W., and R. J. Blakely, HYPERMAG, an interactive, 2- and 2 1/2-dimensional gravity and magnetic modeling program: Version 3.5, *U.S. Geol. Surv. Open File Rep.*, *93-287*, 1–41, 1993.

Satake, K., K. Shimazaki, Y. Tsuji, and K. Ueda, Time and size of a giant earthquake in Cascadia inferred from Japanese tsunami record of January 1700, *Nature*, *379*, 246–249, 1996.

Snavely, P. D., N. S. MacLeod, and H. C. Wagner, Tholeiitic and alkalic basalts of the Eocene Siletz River volcanics, Oregon Coast Range, *Am. J. Sci.*, *266*, 454–481, 1968.

Spence, G. D., R. M. Clowes, and R. M. Ellis, Seismic structure across the active subduction zone of western Canada, *J. Geophys. Res.*, *90*, 6754–6772, 1985.

Stanley, D., and A. Villaseñor, Models of downdip frictional coupling for the Cascadia megathrust, *Geophys. Res. Lett.*, *27*, 1551–1554, 2000.

Stanley, D., A. Villaseñor, and H. Benz, Subduction zone and crustal dynamics of western Washington: A tectonic model for earthquake hazards evaluation, U.S. Department of the Interior, *U.S. Geol. Surv. Open File Rep.*, *99-311*, 135 pp., 1999.

Symons, N. P., and R. S. Crosson, Seismic velocity structure of the Puget Sound region from three-dimensional nonlinear tomography, *Geophys. Res. Lett.*, *24*, 2593–2596, 1997.

Taber, J. J., and B. T. R. Lewis, Crustal structure of the Washington continental margin from refraction data, *Bull. Seismol. Soc. Am.*, *76*, 1011–1024, 1986.

Talwani, M., J. L. Worzel, and M. Landisman, Rapid gravity computations for two-dimensional bodies with application to the Mendocino submarine fracture zone, *J. Geophys. Res.*, *64*, 49–59, 1959.

Tréhu, A. M., I. Asudeh, T. M. Brocher, J. H. Luetgert, W. D. Mooney, J. L. Nabelek, and Y. Nakamura, Crustal architecture of the Cascadia forearc, *Science*, *266*, 237–243, 1994.

Tréhu, A. M., T. M. Brocher, K. Creager, M. Fisher, L. Preston, G. Spence, and the SHIPS 98 Working Group, Geometry of the subducting Juan de Fuca plate: New constraints from SHIPS98, *Geol. Surv. Can.Open File Rep.*, *4350*, 25–32, 2002.

Van Wagoner, T. M., R. S. Crosson, K. C. Creager, G. Medema, L. Preston, N. P. Symons, and T. M. Brocher, Crustal structure and relocated earthquakes in the Puget Lowland, Washington, from high-resolution seismic tomography, *J. Geophys. Res.*, *107*(B12), 2381, doi:10.1029/2001JB000710, 2002.

Wang, K., Simplified analysis of horizontal stresses in a buttressed forearc sliver at an oblique subduction zone, *Geophys. Res. Lett.*, *23*, 2021–2024, 1996.

Weaver, C. S., and G. E. Baker, Geometry of the Juan de Fuca plate beneath Washington and northern Oregon from seismicity, *Bull. Seismol. Soc. Am.*, *78*, 264–275, 1988.

Wells, R. E., C. S. Weaver, and R. J. Blakely, Fore-arc migration in Cascadia and its neotectonic significance, *Geology*, *26*, 759–762, 1998.

Wheeler, J. O., A. J. Brookefield, H. Gabrielse, J. W. H. Monger, H. W. Tipper, and G. J. Woodsworth, Terrane map of the Canadian Cordillera, *Map 1713A*, scale 1:2,000,000, Geol. Surv. of Can., Ottawa, 1989.

White, R. S., D. McKenzie, and R. K. O'Nions, Oceanic crustal thickness from seismic measurements and rare earth element inversions, *J. Geophys. Res.*, *97*, 19,683–19,715, 1992.

Yorath, C. J., A. G. Green, R. M. Clowes, A. S. Brown, M. T. Brandon, E. R. Kanasewich, R. D. Hyndman, and C. Spencer, Lithoprobe, southern Vancouver Island: Seismic reflection sees through Wrangellia to the Juan de Fuca Plate, *Geology*, *13*, 759–762, 1985.

Zelt, C. A., Modelling strategies and model assessment for wide-angle seismic traveltime data, *Geophys. J. Int.*, *139*, 183–204, 1999.

Zelt, C. A., and R. B. Smith, Seismic traveltime inversion for 2-D crustal velocity structure, *Geophys. J. Int.*, *108*, 16–34, 1992.

Zelt, B. C., R. M. Ellis, R. M. Clowes, and J. A. Hole, Inversion of three-dimensional wide-angle seismic data from the southwestern Canadian Cordillera, *J. Geophys. Res.*, *101*, 8503–8529, 1996.

Zelt, B. C., R. M. Ellis, C. A. Zelt, R. D. Hyndman, C. Lowe, G. D. Spence, and M. A. Fisher, Three-dimensional crustal velocity structure beneath the strait of Georgia, British Columbia, *Geophys. J. Int.*, *144*, 695–712, 2001.

——————————

P. Charvis, J. Y. Collot, and D. Graindorge, UMR Géosciences Azur, Observatoire Océanologique de Villefranche sur Mer, B.P. 48, Quai de la Darse, F-06235 Villefranche sur Mer, France. (charvis@ccrv.obs-vlfr.fr; collot@obs-vlfr.fr; david.graindorge@obs-vlfr.fr)

R. Hyndman, Pacific Geoscience Center, Geological Survey of Canada, Box 6000, Sidney, British Columbia, Canada V8L4B2. (hyndman@pgc.nrcan.gc.ca)

G. Spence, School of Earth and Ocean Sciences, University of Victoria, Victoria, British Columbia, Canada V8W 2Y2. (gspence@uvic.ca)

A. M. Tréhu, College of Oceanic and Atmospheric Sciences, Oregon State University, 104 Ocean Administration Building, Corvallis, OR 97331-5503, USA. (tréhu@oce.orst.edu)

Figure 5. (opposite) Northern velocity model. (a) Ray diagrams for the modeled phases and the corresponding observed travel times for stations 1 and 6, 3 and 7, 4 and 8, and 5. The black curves represent calculated travel times. The crosses represent the picked observed arrivals. Different colors correspond to different phases. (b) Velocity model across the northern Strait of Juan de Fuca. Triangles at the top of each velocity model indicate the position of land recording stations. $Pr1$ and $Pr2$ refer to wide-angle deep reflectors. Solid circles with white numbers indicate layer numbers given in text. Solid circles with white letters show the position of seismicity (A, B, C), and gravity sections (A, B) perpendicular to the model and shown in Figures 12–14. (c) Number of ray hits for the northern model, which indicates the ray coverage within the model. White color identifies a number of hits greater than 200.
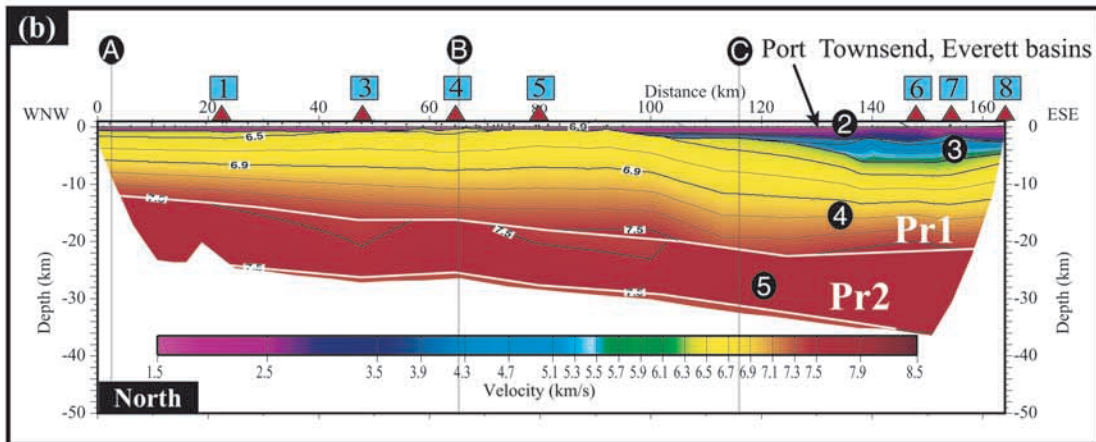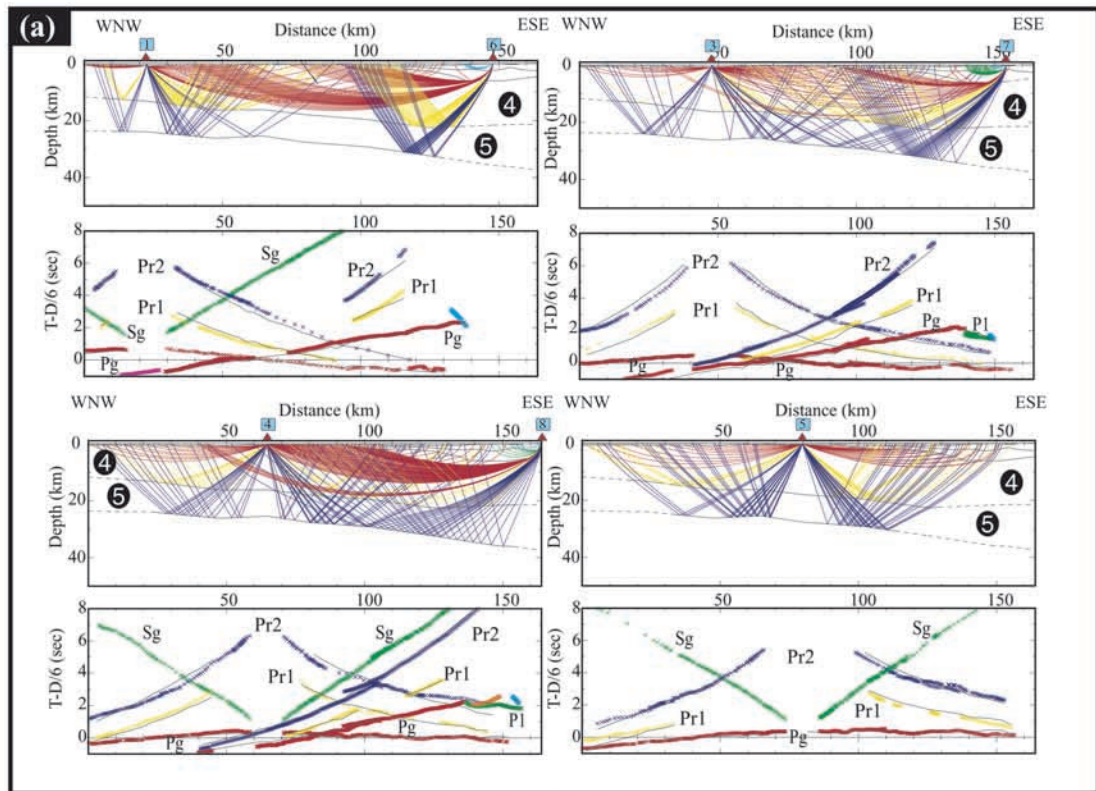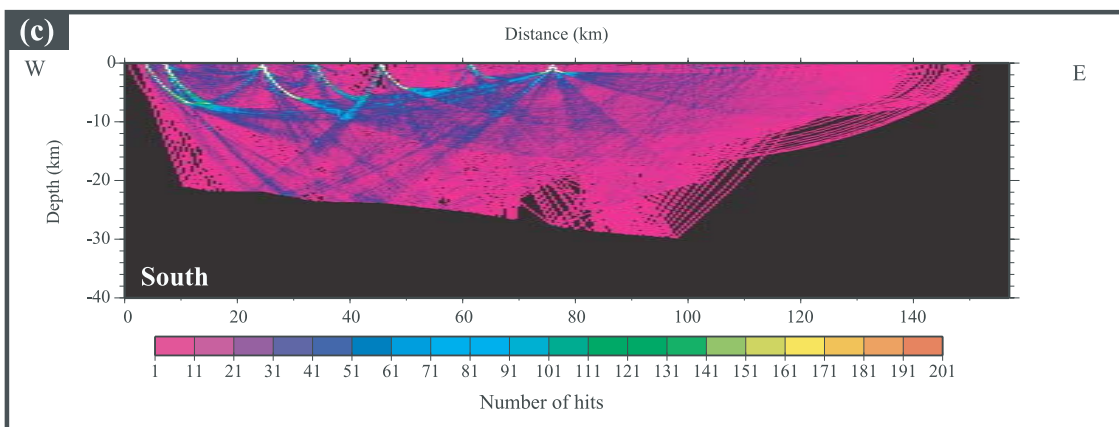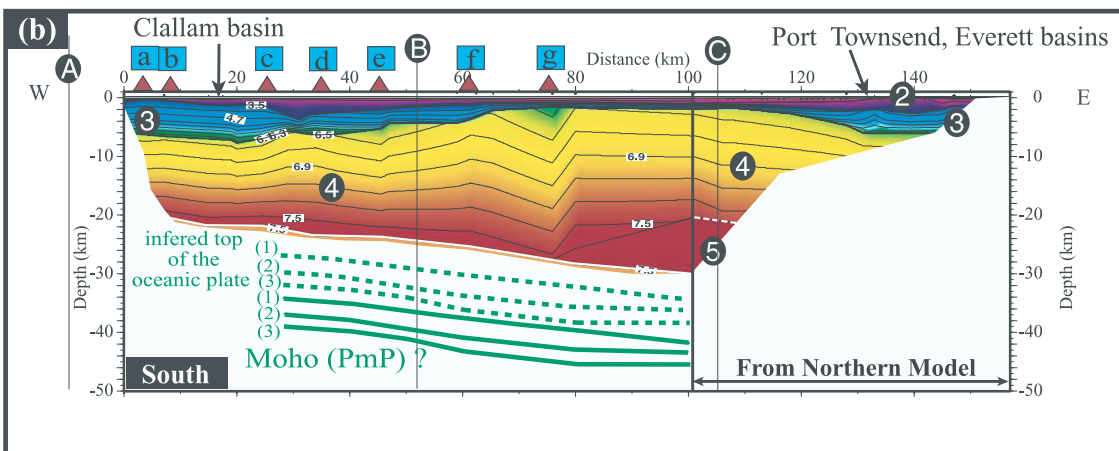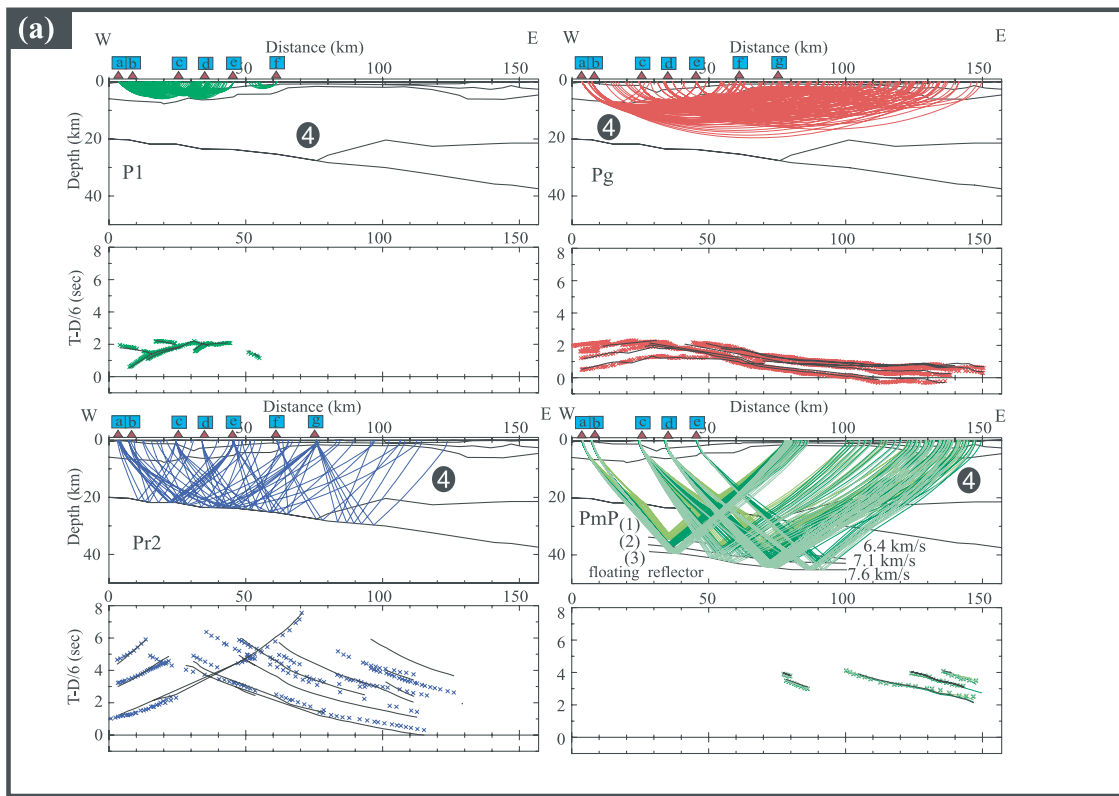
Figure 10. (opposite) Southern velocity model. (a) Ray diagrams for the different modeled phases and the corresponding observed travel times for stations which record different arrivals. The black curves represent calculated travel times. The crosses represent the picked observed arrivals. Different colors correspond to different phases. (b) Velocity model across the southern Strait of Juan de Fuca. Triangles at the top of each velocity model indicate the positions of land recording stations. *Pr*2 refers to wide-angle deep reflectors. Solid circles with white numbers indicate layer numbers. Solid circles with white letters show the position of seismicity and gravity sections (A, B, C), perpendicular to the model and shown in Figures 12–14. For the southern model, Moho depths (green lines) are obtained by modeling of *PmP* arrival times, using a velocity between *Pr*2 and Moho of either 6.4 km s^{-1} (1), 7.1 km s^{-1} (2), or 7.6 km s^{-1} (3). The eastern part of the southern model, between ∼100 and 158 km, is identical to the northern model. (c) Number of ray hits for the northern model which translates the ray coverage within the model. White color identifies a number of hits greater than 200.
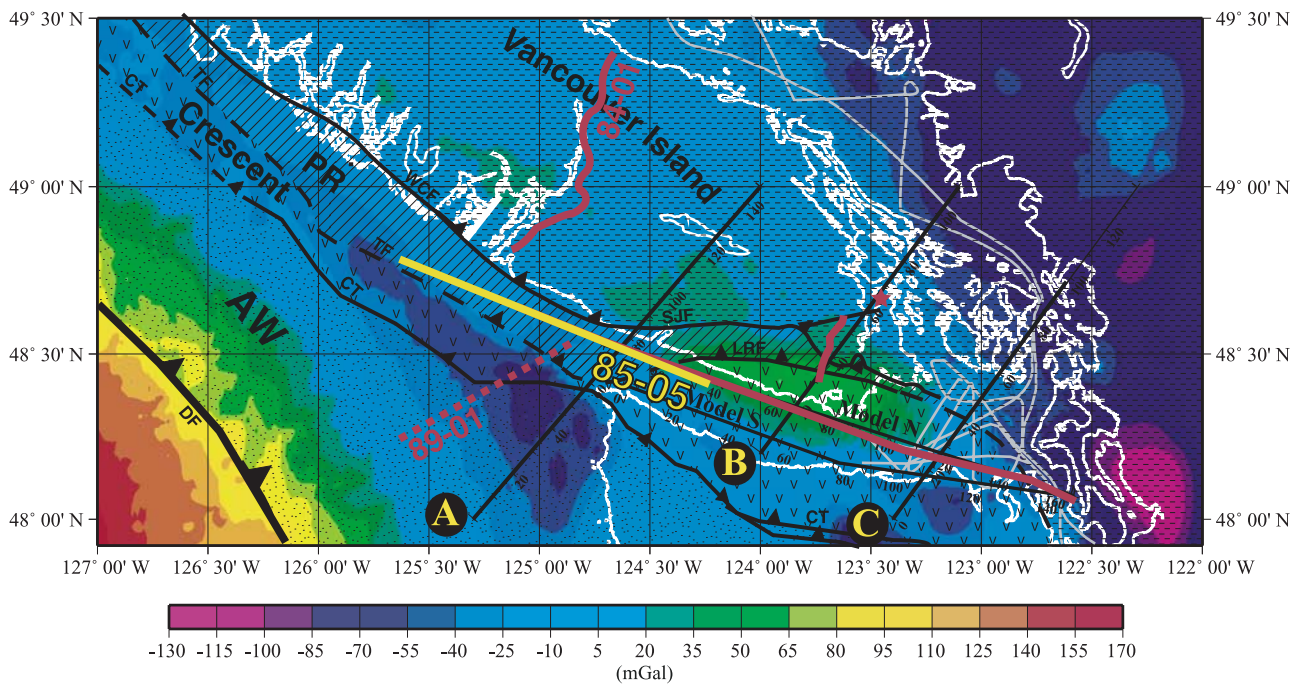
Figure 13. Gravity map of the Strait of Juan de Fuca. Data were interpolated to a grid with a grid size of 0.3 × 0.3 min. The three black lines (A, B, and C) indicate the location of modeled gravity profiles (A and B) (Figure 14) and three seismicity sections (A, B, and C) (Figure 12). Shaded lines show location of SHIPS line in Georgia Strait and eastern Juan de Fuca Strait.